Chemical Geology
March 2023, Volume 620, Pages 121339 (11p.)
https://doi.org/10.1016/j.chemgeo.2023.121339
https://archimer.ifremer.fr/doc/00818/93025/

Magnetic properties of gas hydrate-bearing sediments and their association with iron geochemistry in the Sea of Marmara, Turkey

Yang Hailin [1, 2, *], Zhang Peng [3], Lu Hailong [1, *], Shi Meinan [4], Li Jianming [5], Lu Yinghan [1], Liu Yujia [1], Ruffine Livio [6], Poulton Simon W. [2]

[1] Beijing International Center for Gas Hydrate, School of Earth and Space Sciences, Peking University, Beijing 100871, China
[2] School of Earth and Environment, University of Leeds, Leeds LS2 9JT, UK
[3] State Key Laboratory of Loess and Quaternary Geology, Institute of Earth Environment, Chinese Academy of Sciences, Xi'an 710061, China
[4] School of Ocean Sciences, China University of Geoscience, Beijing 100083, China
[5] Research Institute of Petroleum Exploration and Development, PetroChina, Beijing 100083, China
[6] Ifremer, Univ. Brest, CNRS, UMR Geo-Ocean, F-29280 Plouzané, France

* Corresponding authors : Hailin Yang, email address : hyang@pku.edu.cn ; Hailong Lu, email address : hlu@pku.edu.cn

Abstract :

The anaerobic oxidation of methane, a key geochemical process that is involved in the cycling of sulfate and iron (oxyhydr)oxides in marine sediments, results in the formation of iron sulfides. Although ferrimagnetic iron sulfides have been identified in seepage systems, the link between iron migration and sediment magnetic properties remains poorly understood. Here, we investigate two cores from the Sea of Marmara to evaluate biogeochemical iron cycling and iron sulfide mineralogy in gas hydrate-bearing sediments. Magnetic analyses indicate the presence of greigite and pyrrhotite in a core from a hydrate-rich site with a high hydrocarbon flux, which contrasts with a lack of these minerals in a core characterized by only mild seepage. This is supported by the results of rock magnetic and scanning electron microscope analyses of the sediments. The presence of authigenic greigite is critical for assessing local redox records and together with the occurrence of monoclinic pyrrhotite may suggest specific diagenetic processes in gas hydrate environments. Our analysis demonstrates the usefulness of these ferrimagnetic minerals, with a high saturation isothermal remanent magnetization to magnetic susceptibility ratio (SIRM/χ > 15 kAm−1) and a high index of hysteresis parameters (DJH > 0.2) indicative of magnetic mineralogy changes, for evaluating variability in the intensity of seepage fluxes and for estimating gas hydrate distributions.

Highlights

► Two sediment cores with a similar original terrigenous source have contrasting magnetic properties. ► A reducing and strong flux environment caused iron-driven AOM and formation of authigenic magnetic minerals in the sediments. ► Greigite and monoclinic pyrrhotite are identified as the major magnetic minerals formed in hydrate-bearing sediments.

Keywords : Iron geochemistry, Magnetic properties, Sea of Marmara, Seepage activity, Gas hydrate, Sediments

1. Introduction

The nature of iron sulfide minerals formed during diagenesis (*e.g.*, pyrite (FeS_2), greigite (Fe_3S_4), pyrrhotite ($Fe_{1-x}S$)) in gas hydrate-bearing systems commonly exerts a significant influence on the magnetic properties of associated marine sediment (Bertolin et al., 1995; Roberts and Weaver, 2005; Horng and Roberts, 2006; Merinero et al., 2008; Roberts, 2015; Kars and Kodama, 2015; Zheng et al., 2016). In such sediments, the rate of anaerobic oxidation of methane (AOM) tends to correlate positively with the upward migrating methane flux (Borowski et al., 2013), with sulfate reduction coupled to AOM (sulfate-AOM) producing hydrogen sulfide that reacts with Fe^{2+} to form the iron sulfide minerals (Jørgensen, 1990; Mazumdar et al., 2012; Horng, 2018). In these reactions, dissolved ferrous iron is a key reactant and its availability is controlled by local redox conditions (Lim et al., 2011; Lin et al., 2016). Compared with sulfate, Fe (oxyhydr)oxides are more energetically favorable electron acceptors during AOM, particularly below the sulfate-methane transition zone (SMTZ) in deep-sea sediments (Yang et al., 2021). However, the specific geochemical pathway involving iron during AOM (Fe-AOM) is unresolved, and the origin of the dissolved iron remains unclear (Boetius et al., 2000; Gorlas et al., 2018; Luo et al., 2020).

High pyrite concentrations may occur in the SMTZ, and its preservation in the geological record has been suggested as a possible proxy for sustained methane delivery from deeper sediments (Chen et al., 2006; Lim et al., 2011; Lin et al., 2016). While magnetic minerals, such as iron sulfides and (oxyhydr)oxides, also occur in methane-rich sediments associated with gas hydrates, the nature of this association has not been adequately resolved (Musgrave et al., 2006; Larrasoaña et al., 2007; Lin et al., 2021). The magnetic properties and paleomagnetic signature of host sediments are altered by the characteristics of the iron minerals that form as a result of *in-situ* increases in methane or gas hydrate. Complex interplays of factors, including the availability of dissolved iron, sedimentation rate, and fluid and gas circulation, determine the dissolution and precipitation of iron minerals (Yang et al., 2018; Chen et al., 2021). However, changes in sediment magnetic properties during generation of authigenic iron sulfides from other iron minerals have not been fully explored in either experimental or field studies.

Here, we report magnetic properties for two sediment cores from the Sea of Marmara (SoM), Turkey, combined with high-definition scanning electron microscope observations of iron sulfide minerals and selective geochemical extractions of Fe phases. Our aim is to identify whether ferrimagnetic iron sulfides such as greigite and pyrrhotite are present, and if so, to clarify their

formation and preservation pathways, as well as their potential as indicators of a high methane flux related to the occurrence of gas hydrates.

2. Geological Background and Samples

The SoM is a semi-closed sea connecting the Black Sea to the Mediterranean Sea (Fig. 1). It is located in an area characterized by high seismic activity owing to the presence of the North Anatolian Fault, which facilitates upward fluid migration to the sea floor, and seawater infiltration into the sediment (Ambraseys, 2002; Dupré et al., 2012; Géli et al., 2018; Grall et al., 2018; Henry et al., 2018). The SoM has three main basins – the Tekirdağ and Çınarcık basins in the west and east, respectively, and the Central basin (Okay et al., 2000; Şengör et al., 1985; Sorlien et al., 2012; Çağatay and Uçarkuş, 2019). These basins are separated by two highs – the Western High and the Central High (Fig. 1). Gas emissions are widespread in the SoM, and result from mixing of gases originating from thermogenic, microbial or mantle sources (Géli et al., 2008; Bourry et al., 2009; Burnard et al., 2012; Ruffine et al., 2018a; Ruffine et al., 2018b).

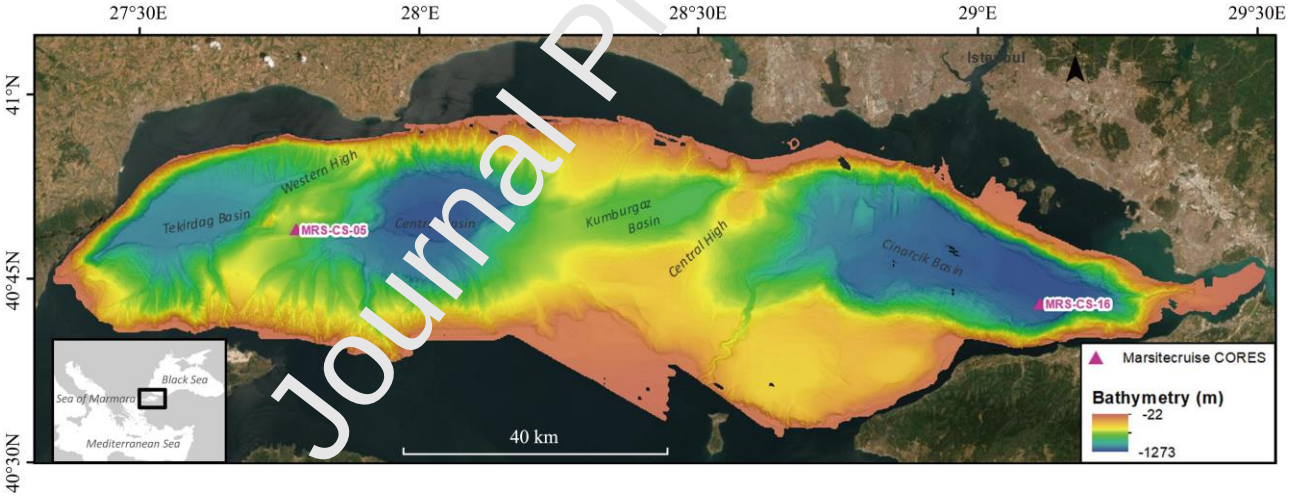

Fig. 1. Location map of the Western High (core MRS-CS-05, where gas hydrates have been discovered) and Çınarcık Basin (core MRS-CS-16, without gas hydrate) in the Sea of Marmara.

Samples were collected during the MarsiteCruise expedition in November 2014 onboard the R/V *Pourquoi Pas?*. Two 10-m-long cores were collected with a piston corer (Calypso®) from the Western High (core MRS-CS-05) and the Çınarcık Basin (core MRS-CS-16) (Fig. 1). After recovery, the cores were cut and sampled in the ship-based laboratory. Subsamples at 1 m intervals were vacuum freeze-dried for subsequent analyses. Gas hydrates were recovered from the Western High,

where hydrate-bound gases are primarily of thermogenic origin, comprising CH_4 (82−87%), heavy hydrocarbons (4.6−8.9%), and relatively high CO_2 concentrations (7.6−8.6%). By contrast, gas hydrate is not present in the Çınarcık Basin, and instead primary microbial gases occur, comprising a high CH_4 concentration (> 99.6%) and trace amounts of heavy hydrocarbons (< 0.01%) and CO_2 (< 0.1%) (Ruffine et al., 2018c).

The sedimentary sequence in core MRS-CS-05 from the Western High consists of an upper marine unit (~0−3.5 mbsf) and an underlying lacustrine unit, whereas the sequence in core MRS-CS-16 from the Çınarcık Basin comprises only the upper marine unit. The marine unit of core MRS-CS-05 is composed of dark green-gray silty clay with total organic matter (TOC) content of 1.7 ± 0.4 wt% and total iron sulfide content of 0.7 ± 0.2 wt%, and the lacustrine unit contains brecciated and soupy structures, which can be attributed to gas hydrate dissociation. The marine unit of core MRS-CS-16 is a hemipelagic greenish-gray mud sequence, with a TOC content of 1.2 ± 0.2 wt% and a total iron sulfide content of 0.5 ± 0.2 wt%, and is interrupted by numerous sandy turbidites and gas expansion voids (Yang et al., 2018; Liu et al., 2019).

The Holocene sedimentation rate is lower in the Western High (~0.2−0.5 m/ka) than in the Çınarcık Basin (~1−2 m/ka; Çağatay et al., 2000; Çağatay et al., 2009; Çağatay et al., 2015). Thus, the core from the Western High records environmental and geological changes through the Late-Pleistocene to Holocene, including a warm/wet climatic period and marine transgression from the Mediterranean at ~12.6 kyr (Major et al., 2002; Vidal, 2010; Eriş et al., 2012; Çağatay et al., 2015). The core from the Çınarcık Basin captures more recent, hemipelagic sedimentation from ~7.7 kyr to the present (Liu et al., 2021).

3. Material and Methods

3.1. Magnetic measurements

Sediment magnetic susceptibility (χ) was measured using a Bartington Instruments MS2 magnetic susceptibility meter. Temperature dependence of low-field magnetic susceptibility (χ-T) was measured in an argon atmosphere using an AGICO MFK1-FA Kappabridge magnetic susceptibility meter. Hysteresis loop and isothermal remanent magnetization (IRM) measurements, limited to a maximum field of 1T, were performed with a MicroMag 3900 alternating-gradient magnetometer. The IRM imparted with a 1T field is referred to as saturation IRM (SIRM). First-order reversal curves (FORCs) were measured (Pike et al., 1999) and FORC diagrams were processed

with the FORCinel software (Harrison and Feinberg, 2008). Low-temperature magnetic measurements were also conducted using a Quantum Design Magnetic Properties Measurement System (MPMS). Housen and Musgrave (1996b) proposed an index D_{JH}, which is the ratio of the hysteresis parameters $(M_{rs}/M_s)/(B_{cr}/B_c)$, to identify magnetic mineralogy changes associated with gas hydrates. M_{rs} is the saturation remanence, M_s is the saturation magnetization, B_{cr} is the remanent coercive field, and B_c is the coercive field.

3.2. Iron speciation and mineral analysis

The sequential extraction procedure of Poulton and Canfield (2005) was used to determine operationally-defined Fe pools. Target phases include Fe carbonates (*e.g.*, siderite and ankerite) extracted with sodium acetate for 24 h (Fe_{carb}); easily reducible Fe (oxyhydr)oxides (*e.g.*, ferrihydrite and lepidocrocite) extracted with hydroxylamine–hydrochloride for 48 h (Fe_{ox1}); reducible, crystalline iron (oxyhydr)oxides (*e.g.*, goethite, akaganeite and hematite) extracted with sodium dithionite for 2 h (Fe_{ox2}), and mixed ferrous-ferric minerals (*e.g.*, magnetite) extracted with ammonium oxalate for 6 h (Fe_{mag}). Fe contents in each extraction solution were determined using inductively coupled plasma optical emission spectrometry (ICP-OES). Bulk Al and Ti contents were determined by ICP-OES after microwave digestion. The concentrations of these elements were within the certified ranges, with precision better than 3%. To provide more detailed information about the main Fe phases extracted in each step, a subsample was investigated by X-ray powder diffraction (PANalytical X'Pert Pro). An additional subsample was used to determine iron sulfide mineral morphology, which was determined using a focused ion beam-scanning electron microscope (FIB-SEM, Helios NanoLab 650) equipped with an energy dispersive X-ray spectrometry (EDS).

4. Results

4.1. Magnetic properties

Low χ values (almost $< 20\times10^{-8}$ m^3/kg) were measured in core MRS-CS-16; while χ for samples from core MRS-CS-05 has higher values (mainly $> 40\times10^{-8}$ m^3/kg), with a maximum value at 400 cmbsf depth (Fig. 2a). SIRM/χ values are generally higher in core MRS-CS-05 relative to core MRS-CS-16 (Fig. 2b). The magnetic index D_{JH} is also higher in samples from core MRS-CS-05 (0.25−0.31) than those in core MRS-CS-16 (average 0.06) (Fig. 2c).

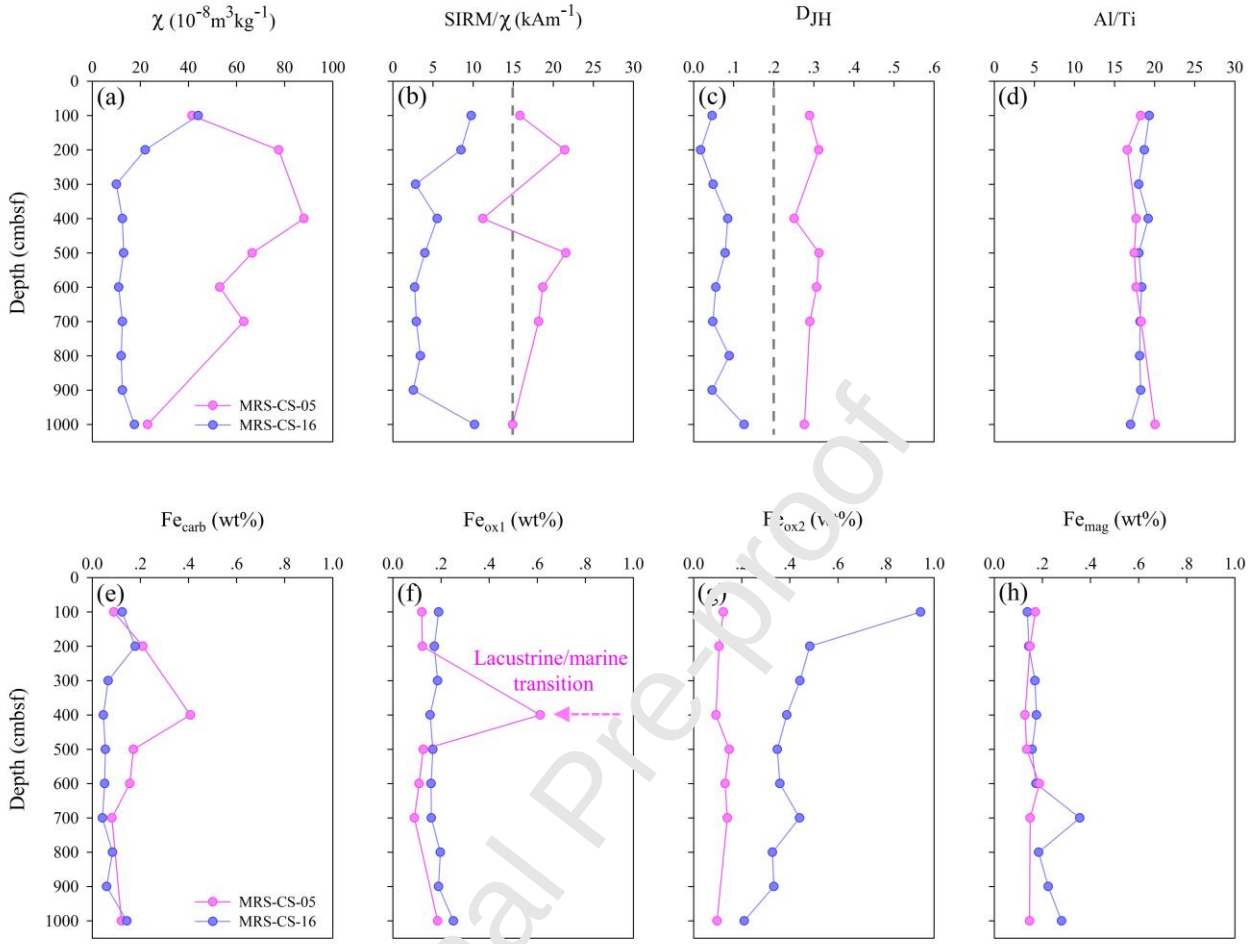

Fig. 2. Downcore magnetic parameters and geochemical trends. **(a)** Magnetic susceptibility (χ), **(b)** SIRM/χ, **(c)** D_{JH} (M_{rs}/M_s versus B_{cr}/B_c), **(d)** Al/Ti ratio, and **(e–h)** operationally-defined Fe phases determined via sequential extraction. The dominant mineral phases in each Fe pool are: Fe_{carb}: siderite; Fe_{ox1}: lepidocrocite; Fe_{ox2}: hematite; and Fe_{mag}: magnetite. Dashed lines in (b) and (c) refer to threshold parameters for identifying ferrimagnetic iron sulfide and gas hydrate occurrences.

χ-T curves (Fig. 3) have different behavior for the two cores. In core MRS-CS-05, the curves for samples from 200 and 600 cmbsf are similar (Fig. 3a, c). Notably, for a sample from 400 cmbsf, the heating curve rises sharply at ~370°C and then decreases and approaches zero at 580°C (Fig. 3b). By contrast, there is no notable difference among χ-T curves for samples from core MRS-CS-16 (Fig. 3d–f).

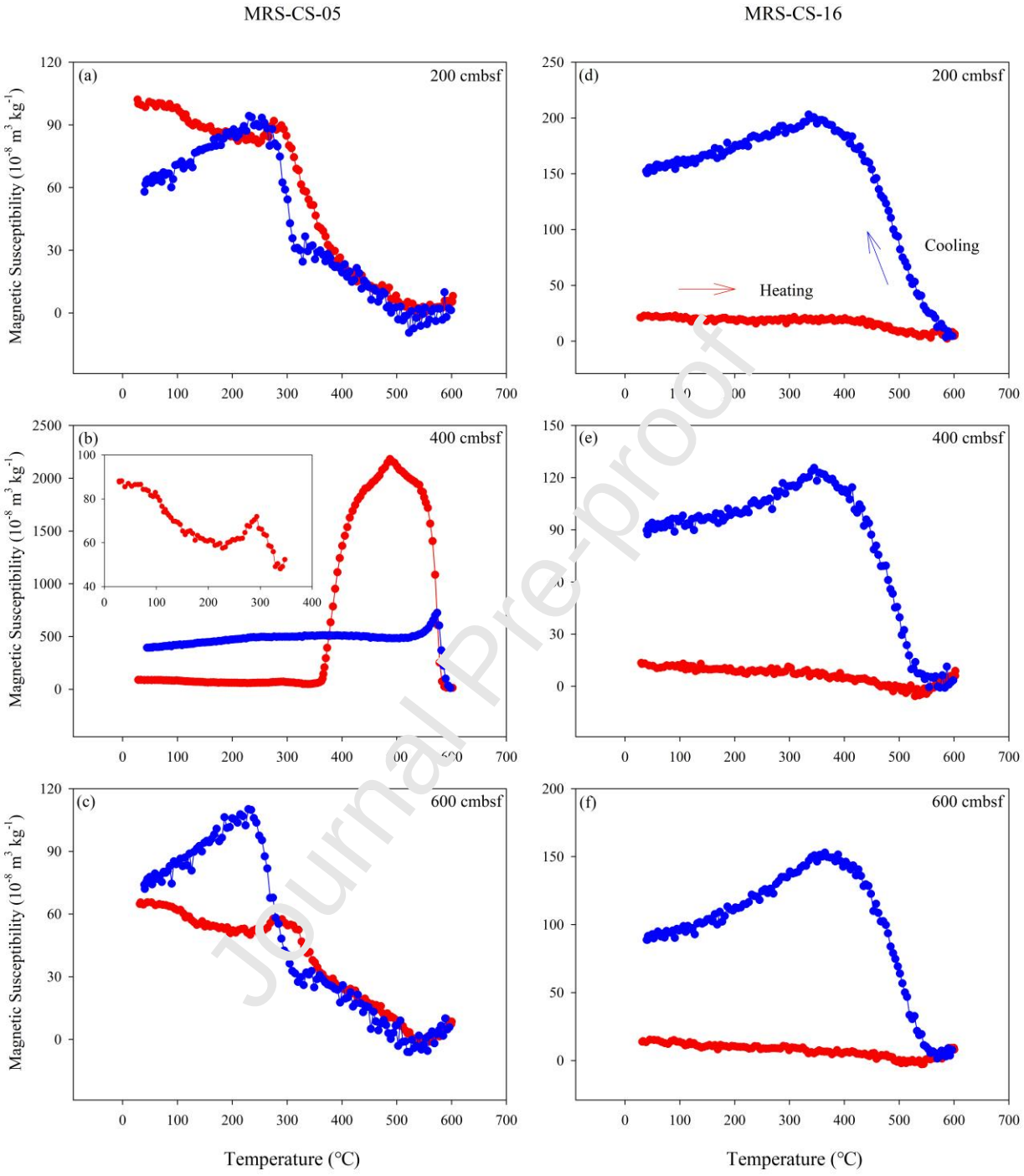

Fig. 3. Magnetic susceptibility versus temperature (χ-T) curves for selected samples from cores MRS-CS-05 **(a−c)** and MRS-CS-16 **(d−f)**. Red and blue lines denote heating and cooling curves, respectively.

Hysteresis loops for samples from two cores are shown in Fig. 4. Hysteresis loops for samples from core MRS-CS-05 have relatively high coercivities and widths, with S-shaped loops (Fig. 4a), while the coercive forces for samples from core MRS-CS-16 are lower, with narrower sigmoidal shaped hysteresis loops (Fig. 4b).

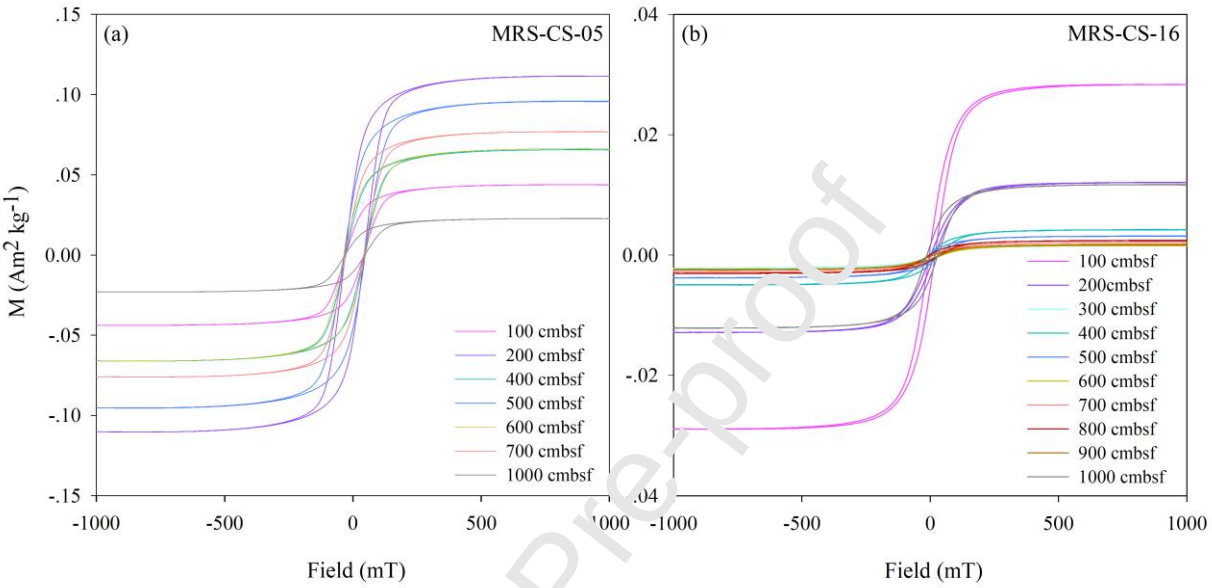

Fig. 4. Hysteresis loops for samples from the two cores from the Sea of Marmara. Results for **(a)** samples from core MRS-CS-05, and **(b)** samples from core MRS-CS-16.

FORC diagrams further confirm the different magnetic properties of the two cores. The closed oval-shaped contours with a central peak in FORC diagrams (Fig. 5a–c) and M_{rs}/M_s (Fig. 5f) demonstrate that samples from MRS-CS-05 contain a high proportion of single domain (SD) greigite (Roberts et al., 2006, 2011).

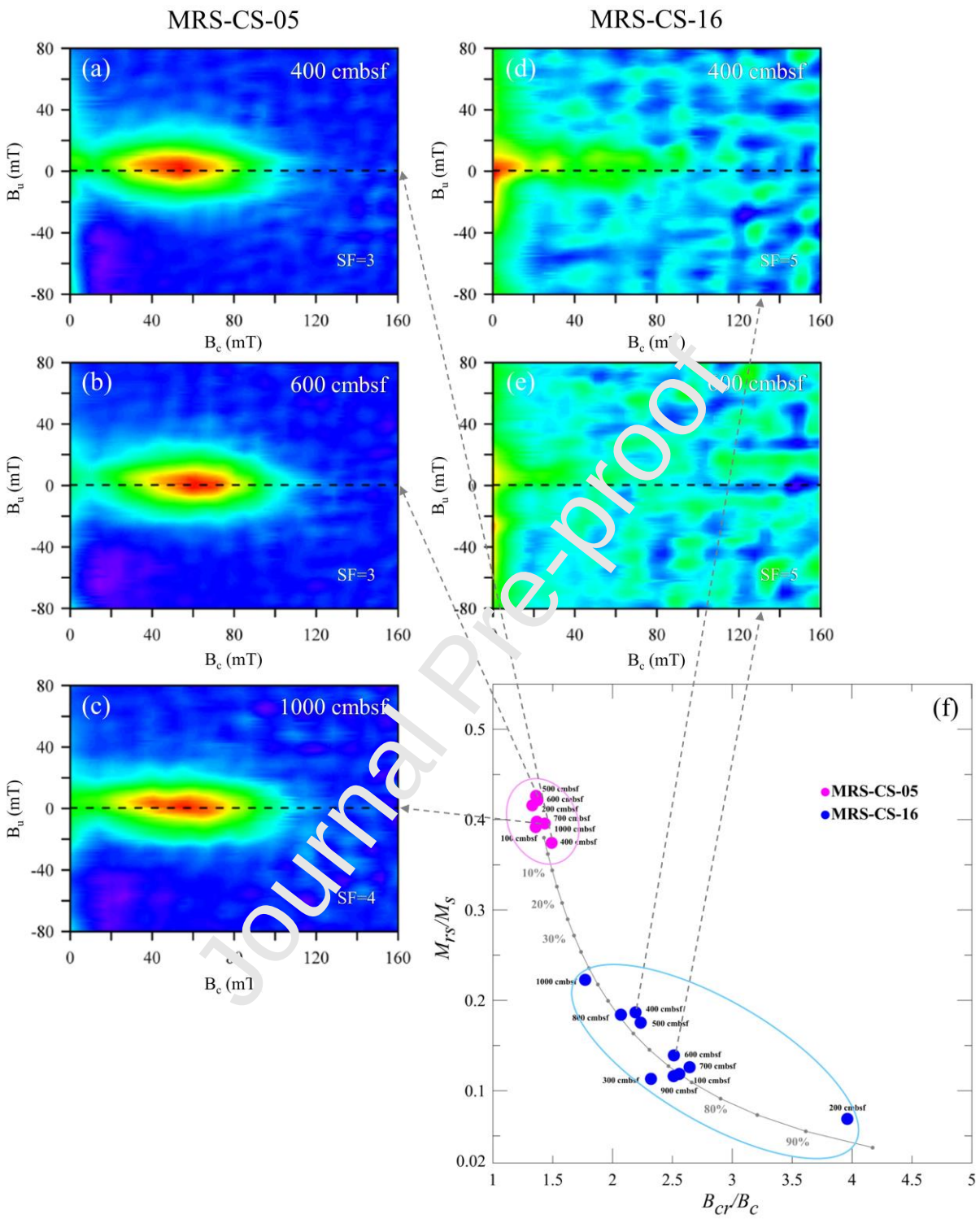

Fig. 5. FORC diagrams and hysteresis ratios plotted on a Day plot (Day et al., 1977). **(a)**, **(b)** and **(c)** Concentric contours and a large vertical spread are indicative of a significant SD contribution in core MRS-CS-05, which contrasts with the results from core MRS-CS-16 in **(d)**, **(e)** and the blue oval zone in **(f)**. B_u: interaction field among particles. SF: smoothing factor.

Moreover, the Besnus transition at ~30−34K is recognizable in ZFC and FC curves for a sample from core MRS-CS-05 (Fig. 6a) due to the presence of monoclinic pyrrhotite (Besnus and Meyer, 1964; Dekkers et al., 1989; Rochette et al., 1990; Horng and Roberts, 2018) and/or siderite (Housen et al., 1996a). However, there is no obvious Besnus transition in other samples from the two cores (Fig. 6b and Fig. S2).

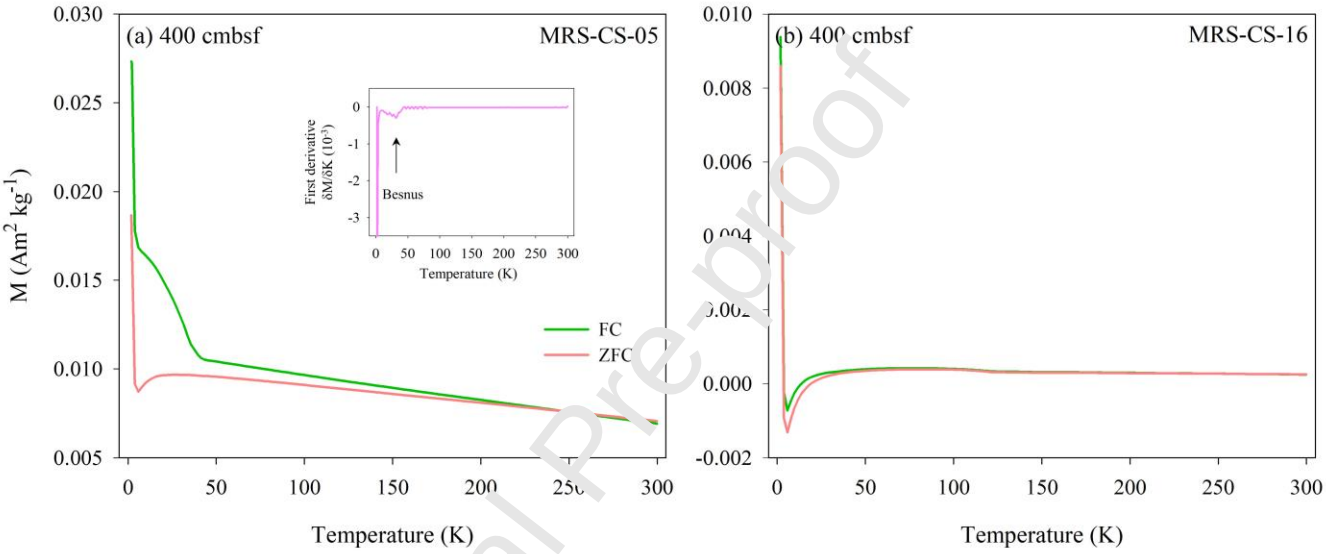

Fig. 6. Zero field-cooled (ZFC) and field-cooled (FC) curves for representative samples from the two cores. Results indicate that **(a)** monoclinic pyrrhotite occurs at 400 cmbsf in core MRS-CS-05, and **(b)** neither a Besnus transition nor a Verwey transition are apparent in curves for a sample from core MRS-CS-16.

4.2 Sediment geochemistry

The Al/Ti ratio in the two cores is approximately 18.2 ± 0.2 wt% (Fig. 1d). Variations in Fe speciation are shown in Fig. 2e−h. Higher Fe_{carb} concentrations generally occur in samples from core MRS-CS-05 (ranging from 0.08 to 0.41 wt%) compared to those from core MRS-CS-16 (< 0.18 wt% (Fig. 1e). Fe_{ox1} concentrations in both cores remain nearly constant at 0.19 ± 0.01 wt%, except for a sample from 400 cmbsf from core MRS-CS-05, where the concentration is 0.61 wt% (Fig. 1f). For Fe_{ox2}, the values in core MRS-CS-05 are relatively stable, with an average of 0.12 ± 0.02 wt%, while in core MRS-CS-16, Fe_{ox2} values are higher than 0.21 wt% and reach a peak of 0.94 wt% at 100 cmsbf (Fig. 1g). The two cores have similar Fe_{mag} values (0.13−0.19 wt%) in the 100−600 cmbsf intervals, with a small increase at the bottom of core MRS-CS-16 (Fig. 1h). The SMTZ was

determined using porewater sulfate data from two additional cores taken close to the sampled cores (Fig. S1) and the results indicate that the present-day SMTZ of the MRS-CS-05 site is close to the sediment-water interface, which contrasts with the relatively deep SMTZ depth of ~200 cmbsf at the MRS-CS-16 site. These SMTZ depths in the Çınarcık Basin and Western High are in agreement with those of previous studies (Çağatay et al., 2004; Tryon et al., 2010).

4.3 FIB-SEM observations

Pyrite is observed by FIB-SEM at several depths in the two cores and can be used to indicate methane activity. Framboidal pyrite represents the dominant pyrite morphology, but a variety of morphologies occur, including isolated or clustered pyrite framboids, cubic and octahedral microcrystals, and irregular pyrite aggregates (Fig. 7a–f).

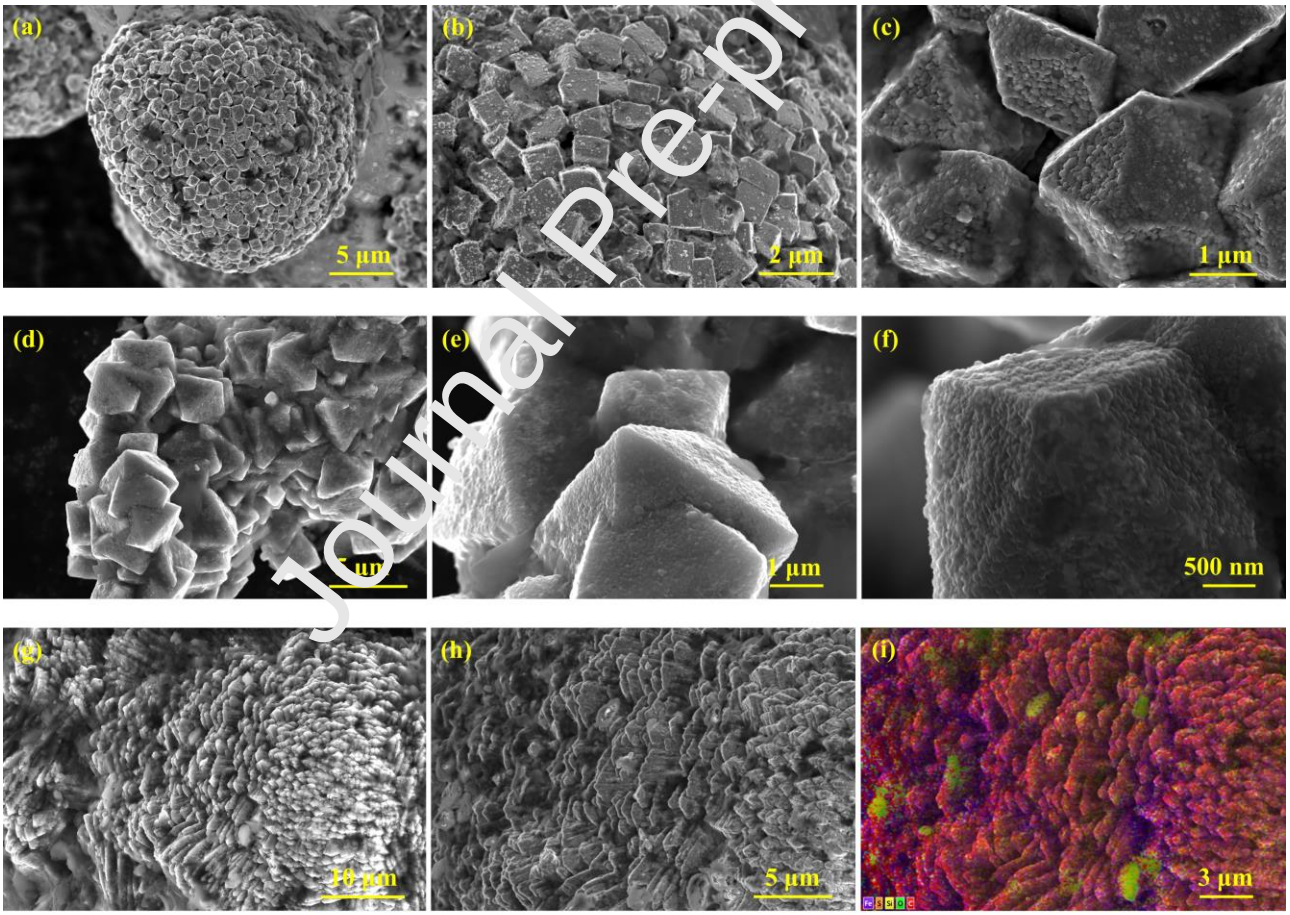

Fig. 7. High-resolution images of pyrite and greigite (analysed by FIB-SEM) in samples from core MRS-CS-05. **(a)**–**(f)** Different pyrite morphologies. Crystal edges in **(c)** and **(f)** may suggest nucleation processes affected by methane seepage. **(g)** and **(h)** Fine-grained SD greigite. **(i)** EDS elemental mapping of greigite in (h).

5. Discussion

5.1. Magnetic mineralogy of the sediment cores

High χ values were observed previously in cores at ~400 cmbsf from the Western High, which are considered to be associated with the lacustrine/marine transition and the sapropel layer (Drab et al., 2015; Makaroğlu et al., 2020). Similar High SIRM/χ values (> 15 kAm^{-1}) in core MRS-CS-05 are potential indicators of ferrimagnetic greigite (Snowball and Thompson, 1988; Roberts, 1995; Chen et al., 2021), which suggests that this mineral may be common in this core. For the sample from 400 cmbsf, the warming curve (Fig. 3b) has a decreasing trend between 300 and 400°C, which probably reflects the occurrence of ferrimagnetic greigite and/or pyrrhotite (Maher and Thompson, 1999; Roberts et al., 2011). Another peak at ~480°C that subsequently decreases to zero at 580°C indicates the Curie temperature of magnetite, which we attribute to the transformation of greigite to magnetite at and above ~370°C during heating (Table S1, Dunlop and Özdemir, 1997). The Besnus transition at 32K by the first derivative (Fig. 6a), approximate reversible heating and cooling curves with a Curie temperature of ~320°C (Fig. 3a–c), and markedly high Mrs/Ms values and low Bcr/Bc values all suggest that monoclinic 4C pyrrhotite is present, rather than its polytype hexagonal 3T pyrrhotite or siderite (35−38K) (Dekkers, 1989; Frederichs et al., 2003; Roberts, 2015; Horng, 2018). Magnetic property measurements, together with FIB-SEM-EDS imaging, provide evidence that SD-sized greigite is the primary remanence carrier in core MRS-CS-05. These magnetic anomalies are consistent with the finding that high D_{JH} values (> 0.2) are indicative of gas hydrates (Housen and Musgrave 1996b; Kars and Kodama, 2015).

5.2. Factors affecting magnetic characteristics

Al and Ti, which are conservative elements during chemical weathering and diagenesis (Nesbitt and Markovics, 1997; Wei et al., 2003), are commonly used to estimate the abundance of terrigenous material in sedimentary environments (Murray and Leinen, 1996). The relatively consistent and stable Al/Ti ratios suggest a similar detrital origin for the two cores. Hence, the variability in iron speciation, as a redox sensitive proxy, dominantly reflects differences in local redox conditions and Fe mineral transformations, rather than variability in the detrital mineral input. Authigenic greigite and pyrrhotite in core MRS-CS-05 (Fig. 3a−c, Fig. 5a−c, Fig. 6a, Fig.7g−i) are intermediate mineral phases during the formation of pyrite (Gagnon et al., 1995; Roberts and Weaver, 2005). Framboidal

pyrite can form in syn- and early-diagenesis and its precise morphology may reflect specific environmental and geochemical parameters (Wilkin et al., 1996; Çağatay et al., 2004; Chang et al. 2020). A peak in pyrite concentrations in methane seepage sediments commonly indicates the location of the SMTZ (Larrasoaña et al., 2007; Dewangan et al, 2013). However, because greigite is also widespread throughout the core, the pyrite concentration profile considered in isolation, likely does not indicate the present-day SMTZ position.

Previous studies suggest that under appropriate conditions, such as during rapid sedimentation with an associated upward SMTZ shift, preservation of greigite rather than pyrite may dominate in continental margin sediments (Greve et al., 2021). The sedimentation rate and SMTZ in the Western High (MRS-CS-05) is lower than that in the Çınarcık Basin (MRS-CS-16) (Çağatay et al., 2004), so magnetic mineral diagenesis in core MRS-CS-05 is more likely linked to a strong fluid flux due to gas hydrate dissociation, with the SMTZ occurring close to the seafloor. Indeed, near seafloor gas hydrate formation and decomposition were previously reported from the Western High by Tryon et al. (2010) and Ruffine et al. (2018b, c), which also plays a key role in pore-water salinity, which in turn is likely to be an important controlling factor during greigite preservation (Chen et al., 2021). However, the abrupt increase in Fe_{carb} and Fe_{ox1} minerals (Fig. 2e, f) and the decrease in greigite (Fig. 2b) at ~400 cmbsf in core MRS-CS-05 are mainly due to the low-salinity and sulfate-limited lacustrine conditions in the Sea of Marmara before ~12.6 ka.

5.3. Iron pools and pathways

During Fe mineral diagenesis, the magnetic characteristics of core MRS-CS-05 changed dramatically, due to the formation and preservation of authigenic greigite and pyrrhotite. Although the two cores have similar Fe concentrations in the Fe_{mag} pool (with a possible slight relative increase in the deeper sediments of core MRS-CS-16; Fig. 2h), magnetite may not contribute significantly to the magnetic susceptibility because of the reducing sedimentary conditions, as discussed below. In addition, the ferric-Fe pools (i.e., Fe_{ox1} and Fe_{ox2}, which dominantly comprise lepidocrocite and hematite, respectively) generally have low and stable concentrations in core MRS-CS-05, with the exception of the peak in Fe_{ox1} linked to the development of lacustrine conditions with sulfate limitation (Fig. 2f). These low concentration ferric-Fe pools are accompanied by the presence of reduced non-sulfidic Fe phases in the Fe_{carb} pool (*e.g.*, siderite; Fig. 2e), and Fe sulfides such as greigite, pyrrhotite and pyrite (Fig. 3a–c, Fig. 5a–c, Fig. 6a, Fig.7g–i). We conclude that the primary

reactive iron (oxyhydr)oxides in MRS-CS-05 were subjected to strongly reducing and acidic conditions, which were associated with upward migrating hydrate-bound gases and methanogenesis, thus producing dissolved Fe(II), which subsequently formed iron sulfide minerals, thereby dramatically changing the sediment magnetic properties .

The above observations indicate that the occurrence and preservation of greigite and pyrrhotite in marine sediments has important implications for the interpretation of magnetic records. Two scenarios can be considered to explain the magnetic properties and iron mineralogy in the two cores (Fig. 8). Scenario A involves methane production and consumption during early diagenesis, where sulfate-driven AOM results in the precipitation of pyrite and calcite (which is precipitated preferentially over siderite). This scenario may result in low Fe$_{ca}$ concentrations (*e.g.*, Fig. 2e) and the weak magnetism observed for core MRS-CS-16. Here, detrital iron (oxyhydr)oxides (*e.g.*, hematite) may be the main contributor to the χ values (Table S2, r = 0.872).

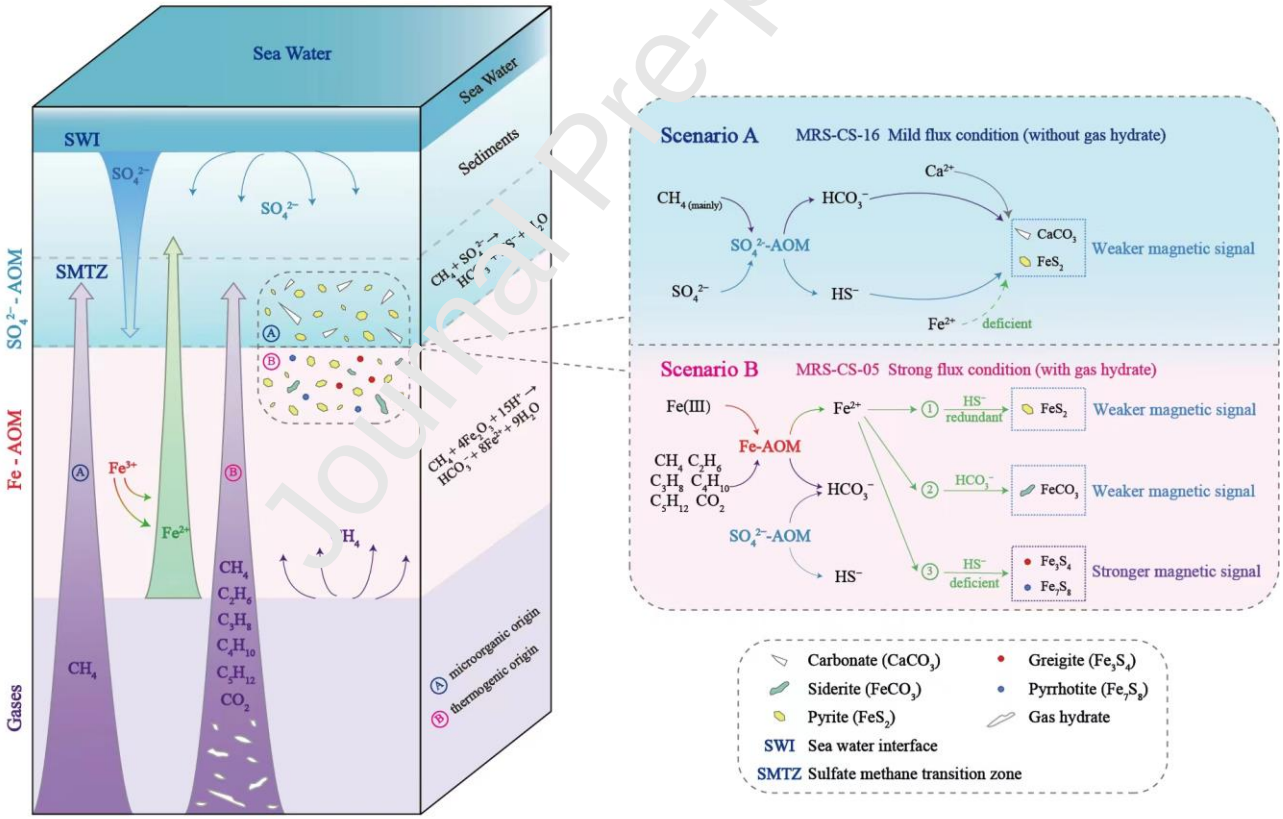

Fig. 8. Two scenarios involving different iron geochemical pathways that may explain the magnetic properties and mineralogy observed in the two cores. Scenario A is the most common in a methane seepage environment, with paramagnetic iron sulfides formed in sediments due to sulfate-AOM. Scenario B proposes Fe-AOM as a significant

factor associated with reductive dissolution of Fe (oxyhydr)oxides, which results in the precipitation of sulfide minerals such as greigite and pyrrhotite, with a major change in the local magnetic characteristics.

In scenario B, post-depositional processes in gas hydrate sediments are affected by a strong hydrocarbon flux. The associated fluids, with high CO_2 concentrations and heavy hydrocarbons, exert a strong influence on redox conditions and pH, thereby enhancing the dissolution of detrital iron (oxyhydr)oxides, as observed in core MRS-CS-05 (Fig. 2f, g). The dissolved Fe(II) results in different potential geochemical pathways (1, 2 and 3 in Fig. 8). If HS^- and HCO_3^- from AOM are abundant, pyrite and siderite are the dominant phases formed, with little change in magnetic properties (pathways 1 and 2). However, when the SMTZ is located near the seafloor, HS^- is deficient in porewaters, leading to greigite and pyrrhotite formation. This provides an explanation for the down-core magnetic property evolution of core MRS-CS-05 (pathway 3). Under such conditions, Fe-driven AOM (Fe^{III} oxides + CH_4 + $H^+ \rightarrow Fe^{II}$ + HCO_3^- + H_2O) likely exerts a strong influence on the magnetic minerals formed.

6. Conclusions

Magnetic property measurements and geochemical data, combined with electron microprobe imaging, were systematically conducted on two cores from the Sea of Marmara. The presence of authigenic greigite and monoclinic pyrrhotite are inferred in the core from the Western High, which was sampled in a current seepage with abundant gas hydrate distribution. This authigenic mineral suite was formed due to upward-migrating fluids that contain dissolved methane and high concentrations of CO_2 and heavy hydrocarbons. Our findings establish a close relationship between sediment magnetic properties, diagenetic iron cycling, and the presence of gas hydrate. Based on the observed magnetic property changes, specific geochemical iron cycling pathways may explain greigite and pyrrhotite formation. It appears that salinity and hydrogen sulfide are also factors that favor preservation of these iron sulfides. Therefore, rock magnetism combined with geochemical data are promising tools for constraining gas hydrate distributions in both modern and ancient settings.

Declaration of Interests

The authors declare that they have no known competing financial interests or personal relationships that could have appeared to influence the work reported in this paper.

Acknowledgments

We thank Hailiang Dong for editorial assistance, and Andrew P. Roberts, M. Namık Çağatay and two other anonymous reviewers for constructive comments that significantly improved the manuscript. This work was supported by the China Geological Survey Project (DD20189310, DD20190230, DD20221703), the Guangdong Major Project of Basic and Applied Basic Research (2020B0301030003), the Fundamental Research Funds for the Central Universities (2652017129), and China Scholarship Council (202006015014). We greatly appreciate the captain, crew, and help with sampling from the onboard scientists of the *Pourquoi Pas?*.

Data Availability

Data are available in a public archive at https://data.mendeley.com/datasets/g49fnbcm78/3

References

Ambraseys, N., 2002. The seismic activity of the Marmara Sea region over the last 2000 years. Bull. Seismol. Soc. Am. 92, 1−18. http://dx.doi.org/10.1785/0120000843

Bertolin, A., Frizzo, P., Rampazzo, G., 1995. Sulphide speciation in surface sediments of the Lagoon of Venice: A geochemical and mineralogical study. Mar. Geol. 123, 73−86. https://doi.org/10.1016/0025-3227(95)80005-V

Besnus, M.J., Meyer, A.J. 1964. Nouvelles données expérimentales sur le magnétisme de la pyrrhotine naturelle. Paper presented at Proceedings of the International Conference on Magnetism, Nottingham, England, pp. 507−511.

Boetius, A., Ravenschlag, K., Schubert, C.J., 2000. A marine microbial consortium apparently mediating anaerobic oxidation of methane. Nature 407, 623−626. https://doi.org/10.1038/35036572

Borowski, W.S., Rodriguez, N.M., Paull, C.K., UsslerIII, W., 2013. Are ^{34}S-enriched authigenic sulfide minerals a proxy for elevated methane flux and gas hydrates in the geologic record? Mar. Petrol. Geol. 43, 381−395. https://doi.org/10.1016/j.marpetgeo.2012.12.009

Bourry, C., Chazallon, B., Charlou, J-L, Donval, J.P, Ruffine, L., Henry, P., Geli, L., Çagatay, M.N., İnan, S., Moreau, M., 2009. Free gas and gas hydrates from the Sea of Marmara, Turkey: Chemical and structural characterization. Chem. Geol. 264, 197−206. https://doi.org/10.1016/j.chemgeo.2009.03.007

Burnard, P., Bourlange, S., Henry, P., Geli L. Tryon, M.D., Natal'in, B., Sengör, A.M.C., Özeren M.S., Çagatay M.N., 2012. Constraints on fluid origins and migration velocities along the Marmara Main Fault (Sea of Marmara, Turkey) using helium isotopes. Earth Planet. Sci. Lett. 341−344: 68−78. https://doi.org/10.1016/j.epsl.2012.05.042

Çağatay, M.N., Erics, K., Ryan, W.B.F, Sancar, Ü., Polonia, A., Akçer, S., Biltekin, D., Gasperini, L., Görür, N., Lericolais, G., Bard, E., 2009. Late Pleistocene-Holocene evolution of the northern shelf of the Sea of Marmara. Mar. Geol. 265, 87−100. https://doi.org/10.1016/j.margeo.2009.06.011

Çağatay, M.N., Görür, N., Algan, O., Eastoe, C., Tchapalyga, A., Ongan, D., Kuhn, T., Kuşcu, I., 2000. Late Glacial−Holocene palaeoceanography of the Sea of Marmara: Timing of connections with the Mediterranean and the Black Seas. Mar. Geol.167, 191−206. https://doi.org/10.1016/S0025-3227(00)00031-1

Çağatay, M.N., Özcan, M., Güngör, E. 2004. Pore-water and sediment geochemistry in the Marmara Sea (Turkey): Early diagenesis and diffusive fluxes. Geochem. Explor. Env. A. 4, 213−225. https://doi.org/10.1144/1467-7873/04-202

Çağatay, M.N., Uçarkuş, G, 2019. Morphotectonics of the Sea of Marmara: Basins and Highs on the North Anatolian Continental Transform Plate Boundary. In: Duarte, J. (Ed.). Transform Plate Boundaries and Fracture Zones, Elsevier, pp. 397−416. https://doi.org/10.1016/B978-0-12-812064-4.00016-5

Çağatay, M.N., Wulf, S. Guichard, F. Özmaral, A., Henry, P, Gasperini, L., 2015. The tephra record from the Sea of Marmara for the last ca. 70 ka and its palaeoceanographic implications. Mar. Geol. 361: 96−110. https://doi.org/10.1016/j.margeo.2015.01.005

Chang, J., Li, Y., Lu, H., 2022. The Morphological characteristics of authigenic pyrite formed in marine sediments. J. Mar. Sci. Eng., 10, 1533. https://doi.org/10.3390/jmse10101533

Chen, D.F., Feng, D., Su, Z., Song, Z.G., Chen, G.Q., Cathles III, L.M., 2006. Pyrite crystallization in seep carbonates at gas vent and hydrate site. Mater. Sci. Eng. C 26, 602−605. https://doi.org/10.1016/j.msec.2005.08.037

Chen, Y., Zhang, W., Nian, X., Sun, Q., Ge, C., Hutchinson, S.M., Cheng, Q., Wang, F., Chen, J., Zhao, X., 2021. Greigite as an indicator for salinity and sedimentation rate change: Evidence from the Yangtze River Delta, China. J. Geophys. Res. Sol. Ea. 126, e2020JB021085. https://doi.org/10.1029/2020JB021085

Day, R., Fuller, M., Schmidt, V. A., 1977. Hysteresis properties of titanomagnetites: Grain-size and compositional dependence. Phys. Earth Planet. Inter. 13, 260−267. https://doi.org/10.1016/0031-9201(77)90108-X

Dekkers M.J., Mattéi, J.L., Fillion, G., Rochette, P. 1989. Grain-size dependence of the magnetic behavior of pyrrhotite during its low temperature transition at 34 K. Geophys. Res. Lett. 16, 855−858. https://doi.org/10.1029/GL016i008p00855

Dewangan, P., Basavaiah, N., Badesab, F.K., Usapkar, A., Mazumdar, A., Joshi, R., Ramprasad, T., 2013. Diagenesis of magnetic minerals in a gas hydrate/cold seep environment off the Krishna–Godavari basin, Bay of Bengal. Mar. Geol. 340, 57−70. https://doi.org/10.1016/j.margeo.2013.04.016

Drab, L., Carlut, J., Hubert-Ferrari, A., Martinez, P., LePoint, G., El Ouahabi, M., 2015. Palaeomagnetic and geochemical record from cores from the Sea of Marmara, Turkey: Age constraints and implications of sapropelic deposition on early diagenesis. Mar. Geol., 360, 40−54. https://doi.org/10.1016/j.margeo.2014.12.002

Dunlop D.J., Özdemir, Ö., 1997. Rock magnetism: Fundamentals and frontiers. Cambridge University Press, New York.

Dupré, S., Scalabrin, C., Géli, L., Henry, P., Grall, C., Çagatay, N., Imren, C., the MARMESONET Scientific Party Team., 2012. Widespread gas emissions in the Sea of Marmara, results from systematic ship-borne multibeam echosounder water column imageries. 11th International Conference of Gas in Marine Sediments, Nice.

Eriş, K.K., Çağatay, N., Beck, C., Lepinay, B.M.D., Corina, C., 2012. Late-Pleistocene to Holocene sedimentary fills of the Çınarcık basin of the Sea of Marmara. Sediment. Geol. 281, 151−165. https://doi.org/10.1016/j.sedgeo.2012.09.001

Frederichs, T., von Dobeneck, T., Bleil, U., Dekkers, M., 2003. Towards the identification of siderite, rhodochrosite, and vivianite in sediments by their low-temperature magnetic properties. Phys. Chem. Earth 28, 669−679. https://doi.org/10.1016/ S1474-7065(03)00121-9

Gagnon, C., Mucci, A., Pelletier, É., 1995. Anomalous accumulation of acid-volatile sulphides (AVS) in a coastal marine sediment, Saguenay Fjord, Canada. Geochimi. Cosmochimi. Acta 59, 2663−2675. https://doi.org/10.1016/0016-7037(95)00163-T

Géli, L., Henry, P., Grall, C., Tary, J.-B., Lomax, A., Batsi, E., Riboulot, V., Cros, E., Gürbüz, C., Işık, S., 2018. Gas and seismicity within the Istanbul seismic gap. Sci. Rep. 8, 6819. https://doi.org/10.1038/s41598-018-23536-7

Géli, L., Henry, P., Zitter, T., Dupré, S., Tryon, M., Çagatay, M., de Lépinay, B., Le Pichon, X., engör, A., Görür, N., 2008. Gas emissions and active tectonics within the submerged section of the North Anatolian Fault zone in the Sea of Marmara. Earth Planet. Sci. Lett. 274, 34−39. https:/ doi.org/10.1016/j.epsl.2008.06.047

Gorlas, A., Jacquemot, P., Guigner, J-M., Gill, S., Forterre, P., Guyot, F., 2018. Greigite nanocrystals produced by hyperthermophilic archaea of *Thermococcales* order. PLoS One 13, e0201549. https://doi.org/10.1371/journal.pone.0201549

Grall, C., Henry, P., Dupré, S., Géli, L., Scalabrin, C., Zitter, T.A.C., Sengor, A.M.C., Cagatay, M.N., Cifci, G., 2018. Upward migration of gas in an active tectonic basin: An example from the Sea of Marmara. Deep-Sea Res. Pt II 153, 17−35. https://doi.org/10.1016/j.dsr2.2018.06.007

Greve, A., Kars, M., Dekkers, M.J., 2021. Fluid accumulation, migration and anaerobic oxidation of methane along a major splay fault at the Hikurangi subduction margin (New Zealand): A magnetic approach. J. Geophys. Res. Sol. Ea. 126, e2020JB020671. https://doi.org/10.1029/2020JB020671

Harrison, R.J., Feinberg, J.M., 2008. FORCinel: An improved algorithm for calculating first-order reversal curve distributions using locally weighted regression smoothing. Geochem. Geophy. Geosy, 9. https://doi.org/10.1029/2008gc001987

Henry, P., Grall, C., Kende, I., Viseur, S., Özeren, M.S., Şengör, A.M.C., Dupré, S., Saclabrin, C., Géli, L., 2018. A statistical approach to relationships between fluid emissions and faults: The Sea of Marmara case. Deep-Sea Res. Pt II 153, 131−143. https://doi.org/10.1016/j.dsr2.2018.05.010

Horng, C.-S., 2018. Unusual magnetic properties of sedimentary pyrrhotite in methane seepage sediments: Comparison with metamorphic pyrrhotite and sedimentary greigite. J. Geophys. Res. Sol. Ea. 123, 4601−4617. https://doi.org/10.1002/2017JB015262

Horng, C.-S., Roberts, A.P., 2006. Authigenic or detrital origin of pyrrhotite in sediments?: Resolving a paleomagnetic conundrum. Earth Planet. Sci. Lett. 241. 750−762. https://doi.org/10.1016/j.epsl.2005.11.008

Horng, C.-S., Roberts, A.P., 2018. The low-temperature Besnus magnetic transition: Signals due to monoclinic and hexagonal pyrrhotite. Geochem. Geophys. Geosystem. 19, 3364−3375. https://doi.org/10.1029/2017GC007394

Housen, B.A., Banerjee, S.K., Moskowitz, B. M., 1996a. Low temperature magnetic properties of siderite and magnetite in marine sediments. Geophys. Res. Lett. 23, 2843−2846. https://doi.org/10.1029/96GL01197

Housen, B.A., Musgrave, R.J., 1996b. Rock-magnetic signature of gas hydrates in accretionary prisms sediments. Earth Planet. Sci. Lett. 139, 509−519. https://doi.org/10.1016/0012-821X(95)00245-8

Jørgensen, B.B., 1990. A thiosulfate shunt in the sulfur cycle of marine sediments. Science 249, 152−154. https://doi.org/10.1126/science.249.4965.152

Kars, M., Kodama, K., 2015. Authigenesis of magnetic minerals in gas hydrate-bearing sediments in the Nankai Trough, offshore Japan. Geochem. Geophys. Geosystem. 16, 947−961. https://doi.org/10.1002/2014GC005614

Larrasoaña, J. C., Roberts, A. P., Musgrave, R. J., Gràcia, E., Piñero, E., Vega, M., Martínez-Ruize F., 2007. Diagenetic formation of greigite and pyrrhotite in gas hydrate marine sedimentary systems. Earth Planet. Sci. Lett. 261, 350−366. https://doi.org/10.1016/j.epsl.2007.06.032

Lim, Y.C., Lin, S., Yang, T.F., Chen, Y-G., Liu, C.-S., 2011. Variations of methane induced pyrite formation in the accretionary wedge sediments offshore southwestern Taiwan. Mar. Petrol. Geol. 28, 1829−1837. https://doi.org/10.1016/j.marpetgeo.2011.04.004

Lin, Q., Wang, J., Algeo, T.J., Sun, F., Lin, R., 2016. Enhanced framboidal pyrite formation related to anaerobic oxidation of methane in the sulfate-methane transition zone of the northern South China Sea. Mar. Geol. 379, 100−108. https://doi.org/10.1016/j.margeo.2016.05.016

Lin, Z., Sun, X. Roberts, A.P., Strauss, H. Lu, Y. Yang, X. Gong, J. Li, G. Brunner, B. Peckmann, J., 2021. A novel authigenic magnetite source for sedimentary magnetization. Geology 49, 360−365. https://doi.org/10.1130/G48069.1

Liu, Y., Lu, H., Yin, X., Ruffine, L., Çağatay, M.N., Yang, H., Chen, C., He, D., Zhu, Z., Yalamaz, B., 2019. Interpretation of Late-Pleistocene/Holocene transition in the Sea of Marmara from geochemistry of bulk carbonates. Geochem. Geophys. Geosystem. 20: 4487−4504. https://doi.org/10.1029/2019GC008364

Liu, Y., Lu, X., Çağatay, M.N., Zhang, Y., Li, Y., Peng, Y., Ruffine, L., Lu, H., 2021. The organic, inorganic and isotope geochemistry of the holocene sapropel units in the sea of Marmara and their paleoceanographic significance. Mar. Petrol. Geol. 129, 105094. https://doi.org/10.1016/j.marpetgeo.2021.105094

Luo, M., Torres, M.E., Hong, W.L., Pape, T., Fronzek, J., Kutterolf, S., Mountjoy, J.J., Orpin, A., Henkel, S., Huhn, K., Chen. D., Kasten, S., 2020. Impact of iron release by volcanic ash alteration on carbon cycling in sediments of the northern Hikurangi margin. Earth Planet. Sci. Lett. 541, 116288. https://doi.org/10.1016/j.epsl.2020.116288

Maher B.A., Thompson R., 1999. Quaternary Climates, Environments and Magnetism. Cambridge University Press, Cambridge, UK.

Makaroğlu, Ö., Nowaczyk, N.R., Keriş, K.K., Çağatay, M.N., 2020. High-resolution palaeomagnetic record from Sea of Marmara sediments for the last 70 ka. Geophys. J. Int., 222, 2024−2039. https://doi.org/10.1093/gji/ggaa281

Major, C., Ryan, W., Lericolais G., Hajdas, I., 2002. Constraints on black sea outflow to the Sea of Marmara during the last glacial-interglacial transition. Mar. Geol. 190, 19−34. https://doi.org/10.1016/S0025-3227(02)00340-7

Mazumdar, A., Peketi, A., Joao, H., Dewangan, P., Borole, D. V., Kocherla, M., 2012. Sulfidization in a shallow coastal depositional setting: Diagenetic and palaeoclimatic implications. Chem. Geol. 322−323, 68−78. https://doi.org/10.1016/j.chemgeo.2012.06.005

Merinero, R., Lunar, R., Martínez-Frías, J., Somoza, L., Díaz-del-Río, V., 2008. Iron oxyhydroxide and sulphide mineralization in hydrocarbon seep-related carbonate submarine chimneys, Gulf of Cadiz (SW Iberian Peninsula). Mar. Petrol. Geol. 25, 706−713. https://doi.org/10.1016/j.marpetgeo.2008.03.005

Murray, R.W., Leinen, M.,1996. Scavenged excess aluminum and its relationship to bulk titanium in biogenic sediment from the central equatorial Pacific Ocean. Geochim. Cosmochim. Ac. 60, 3869−3878. https://doi.org/10.1016/0016-7037(96)00236-0

Musgrave, R. J., Bangs, N. L., Larrasoaña, J. C., Gràcia, E., Hollarsby, J. A., Vega, M. E., 2006. Rise of the base of the gas hydrate zone since the last glacial recorded by rock magnetism. Geology 34, 117−120. https://doi.org/10.1130/G22008.1

Nesbitt, H.W., Markovics, G., 1997. Weathering of granodioritic crust, long-term storage of elements in weathering profiles, and petrogenesis of siliciclastic sediments. Geochim. Cosmochim. Ac. 61, 1653−1670. https://doi.org/10.1016/S0016-7037(97)00031-8

Wei, G. Liu, Y., Li, X., Shao, L. Liang, X, 2003. Climatic impact on Al, K, Sc and Ti in marine sediments: Evidence from ODP Site 1144, South China Sea. Geochem. J. 37: 593−602. https://doi.org/10.2343/geochemj.37.593

Okay, A. İ., Kaşlılar-Özcan, A., Imren, C., Boztepe-Güney, A., Demirbağ, E., Kuşçu, İ., 2000. Active faults and evolving strike-slip basins in the Marmara Sea, northwest Turkey: A multichannel seismic reflection study. Tectonophysics 321, 189−218. https://doi.org/10.1016/S0040-1951(00)00046-9

Poulton, S., Canfield, D., 2005. Development of a sequential extraction procedure for iron: Implications for iron partitioning in continentally derived particulates. Chem Geol. 214, 209−221. https://doi.org/10.1016/j.chemgeo.2004.09.003

Pike, C.R., Roberts, A.P., Verosub, K.L., 1999, Characterizing interactions in fine magnetic particle systems using first order reversal curves. J. Appl. Phys. 85, 6660−6667. https://doi.org/10.1063/1.370176

Roberts, A.P., 1995. Magnetic properties of sedimentary greigite (Fe_3S_4). Earth Planet. Sci. Lett. 134, 227−236. https://doi.org/10.1016/0012-821X(95)00131-U

Roberts, A.P., 2015. Magnetic mineral diagenesis. Earth Sci. Rev. 151, 1−47. https://doi.org/10.1016/j.earscirev.2015.09.010

Roberts, A.P., Liu, Q., Rowan, C.J., Chang, L., Carvallo, C., Torrent, J., Horng, C.S., 2006. Characterization of hematite (α-Fe_2O_3), goethite (α-FeOOH), greigite (Fe_3S_4), and pyrrhotite (Fe_7S_8) using first-order reversal curve diagrams. J. Geophys. Res. Sol. Ea. 111, B12S35. https://doi.org/10.1029/2006JB004715

Roberts, A.P., Chang, L., Heslop, D., Florindo, F., Larrasoaña, J.C., 2012. Searching for single domain magnetite in the "pseudo-single-domain" sedimentary haystack: Implications of biogenic magnetite preservation for sediment magnetism and relative paleointensity determinations. J. Geophys. Res. Sol. Ea. 117, B8104. https://doi.org/10.1029/2012jb009412

Roberts, A.P., Chang, L., Rowan, C.J., Horng, C.S., Florindo, F., 2011. Magnetic properties of sedimentary greigite (Fe_3S_4): An update. Rev. Geophys. 49, RG1002. https://doi.org/10.1029/2010RG000336

Roberts, A. P., Weaver, R. (2005) Multiple mechanisms of remagnetization involving sedimentary greigite (Fe_3S_4). Earth Planet. Sci. Lett. 231, 263−277. https://doi.org/10.1016/j.epsl.2004.11.024

Rochette P., Fillion, G., Mattéi, J.-L., Dekkers, M.J., 1990. Magnetic transition at 30−34 K in Fe_7S_8: Insight into a widespread occurrence of pyrrhotite in rocks, Earth Planet. Sci. Lett., 98, 319−328. https://doi.org/10.1016/0012-821X(90)90034-U

Ruffine, L., Cagatay, M.N., Geli, L., 2018a. Fluids and processes at the seismically active fault zone in the Sea of Marmara. Deep-Sea Res. Pt II 153, 1−3. https://doi.org/10.1016/j.dsr2.2018.09.011

Ruffine, L., Donval, J.-P., Croguennec, C., Burnard, P., Lu, H., Germain, Y., Legoix, L.N., Bignon, L., Çağatay, M.N., Marty, B., Madre, D., Pitel-Roudaut, M., Henry, P., Géli, L., 2018b. Multiple gas reservoirs are responsible for the gas emissions along the Marmara fault network. Deep-Sea Res. Pt II 153, 48−60. https://doi.org/10.1016/j.dsr2.2017.11.011

Ruffine, L., Ondreas, H., Blanc-Valleron, M.-M., Teichert, B.M.A., Scalabrin, C., Rinnert, E., Birot, D., Croguennec, C., Ponzevera, E., Pierre, C., Donval, J.-P., Alix, A.-S., Germain, Y., Bignon, L., Etoubleau, J., Caprais, J.-C., Knoery, J., Lesongeur, F., Thomas, B., Roubi, A., Legoix, L.N., Burnard, P., Chevalier, N., Lu, H., Dupré, S., Fontanier, C., Dissard, D., Olgun, N., Yang, H., Strauss, H., Özaksoy, V., Perchoc, J., Podeur, C., Tarditi, C., Özbeki, E., Guyader, V., Marty, B., Madre, D., Pitel-Roudaut, M., Grall, C., Embriaco, D., Polonia, A., Gasperini, L., Çağatay, M.N., Henry, P., Géli, L., 2018c. Multidisciplinary investigation on cold seeps with vigorous gas emissions in the Sea of Marmara (MarsiteCruise): Strategy for site detection and sampling and first scientific outcome. Deep-Sea Res. Pt II 153, 36−47. https://doi.org/10.1016/j.dsr2.2018.03.006

Şengör, A., Görür, N., Şaroğlu, F., 1985. Strike-slip faulting and related basin formation in zones of tectonic escape: Turkey as a case study. Strike-slip deformation, basin formation, and sedimentation 227−264. https://doi.org/10.2110/pec.85.37.0227

Snowball. I., Thompson, R., 1988. The occurrence of greigite in sediments from Loch Lomond. J. Quat. Sci. 3, 121−125. https://doi.org/10.1002/jqs.3390030203

Sorlien, C.C., Akhun, S.D., Seeber, L., Steckler, M.S., Shillington, D.J., Kurt, H., Çifçi, G., Poyraz, D.T., Gürçay, S., Dondurur, D., 2012. Uniform basin growth over the last 500 ka, North Anatolian Fault, Marmara Sea, Turkey. *Tectonophysics* 518−521, 1−16. https://doi.org/10.1016/j.tecto.2011.10.006

Tryon, M.D., Henry, Çağatay, M.N., Zitter, T.A.C. Géli, L., Gasperini, L, Burnard P., Bourlange, S., Grall, C., 2010. Pore fluid chemistry of the North Anatolian Fault Zone in the Sea of Marmara: A diversity of sources and processes. Geochem. Geophys. Geosystem. 11. https://doi.org/10.1029/2010GC003177

Vidal, L., Ménot, G., Joly, C., Bruneton, H., Rostek, F., Çağatay, M.N., Major, C., Bard, E., 2010. Hydrology in the Sea of Marmara during the last 23 ka: Implications for timing of black sea connections and sapropel deposition. Paleoceanography 25, PA1205. https://doi.org/10.1029/2009PA001735

Wilkin, R.T., Barnes, H.L., Brantley, S.L., 1996. The size distribution of framboidal pyrite in modern sediments: An indicator of redox conditions. Geochim. Cosmochim. Ac. 60, 3897−3912. https://doi.org/10.1016/0016-7037(96)00209-8

Yang, H., Lu, H., Ruffine, L., 2018. Geochemical characteristics of iron in sediments from the Sea of Marmara. Deep-Sea Res. Pt II 153, 121−130. https://doi.org/10.1016/j.dsr2.2018.01.010

Yang, H., Yu, S., Lu, H., 2021. Iron-coupled anaerobic oxidation of methane in marine sediments: A Review. J. Mar. Sci. Eng. 9, 875. https://doi.org/10.3390/jmse9080875

Zheng, G., Wang, X., Fortin, D., Pan, Y., Liang, M., Wu, D., Yang, R., Fan, X., Zhao, Y., 2016. Sulfur speciation in marine sediments impacted by gas emissions in the northern part of the South China Sea. Mar. Petrol. Geol. 73, 181−187. https://doi.org/10.1016/j.marpetgeo.2016.02.034

Declaration of interests

☒ The authors declare that they have no known competing financial interests or personal relationships that could have appeared to influence the work reported in this paper.

☐ The authors declare the following financial interests/personal relationships which may be considered as potential competing interests:

Highlights

- Two sediment cores with a similar original terrigenous source have contrasting magnetic properties
- A reducing and strong flux environment caused iron-driven AOM and formation of authigenic magnetic minerals in the sediments
- Greigite and monoclinic pyrrhotite are identified as the major magnetic minerals formed in hydrate-bearing sediments

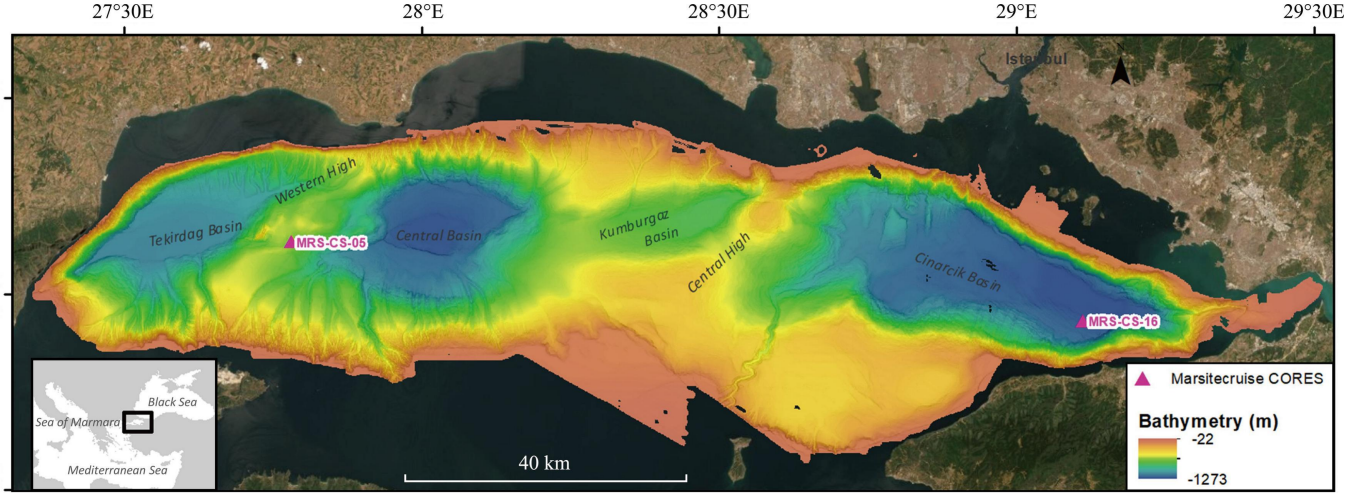
27°30E
28°E
28°30E
29°E
29°30E
41°N
40°45N
40°30N
Istanbul
Western High
Tekirdag Basin
MRS-CS-05
Central Basin
Kumburgaz Basin
Central High
Cinarcik Basin
MRS-CS-16
Black Sea
Sea of Marmara
Mediterranean Sea
40 km
Marsitecruise CORES
Bathymetry (m)
-22
-1273

Figure 1

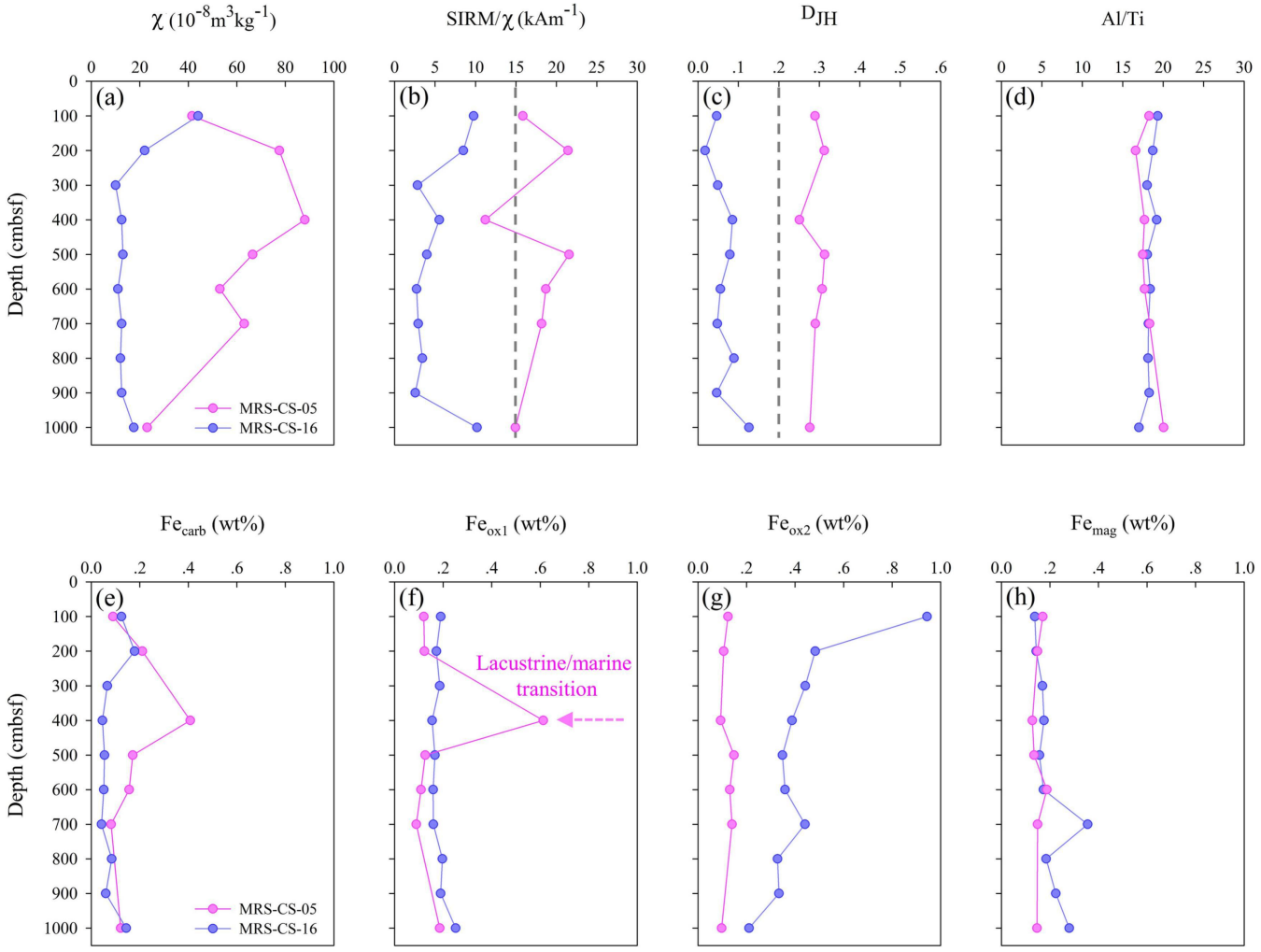
χ (10-8m3kg-1)
SIRM/χ (kAm-1)
DJH
Al/Ti
Depth (cmbsf)
(a)
(b)
(c)
(d)
MRS-CS-05
MRS-CS-16
Fecarb (wt%)
Feox1 (wt%)
Feox2 (wt%)
Femag (wt%)
(e)
(f)
(g)
(h)
Lacustrine/marine transition

Figure 2

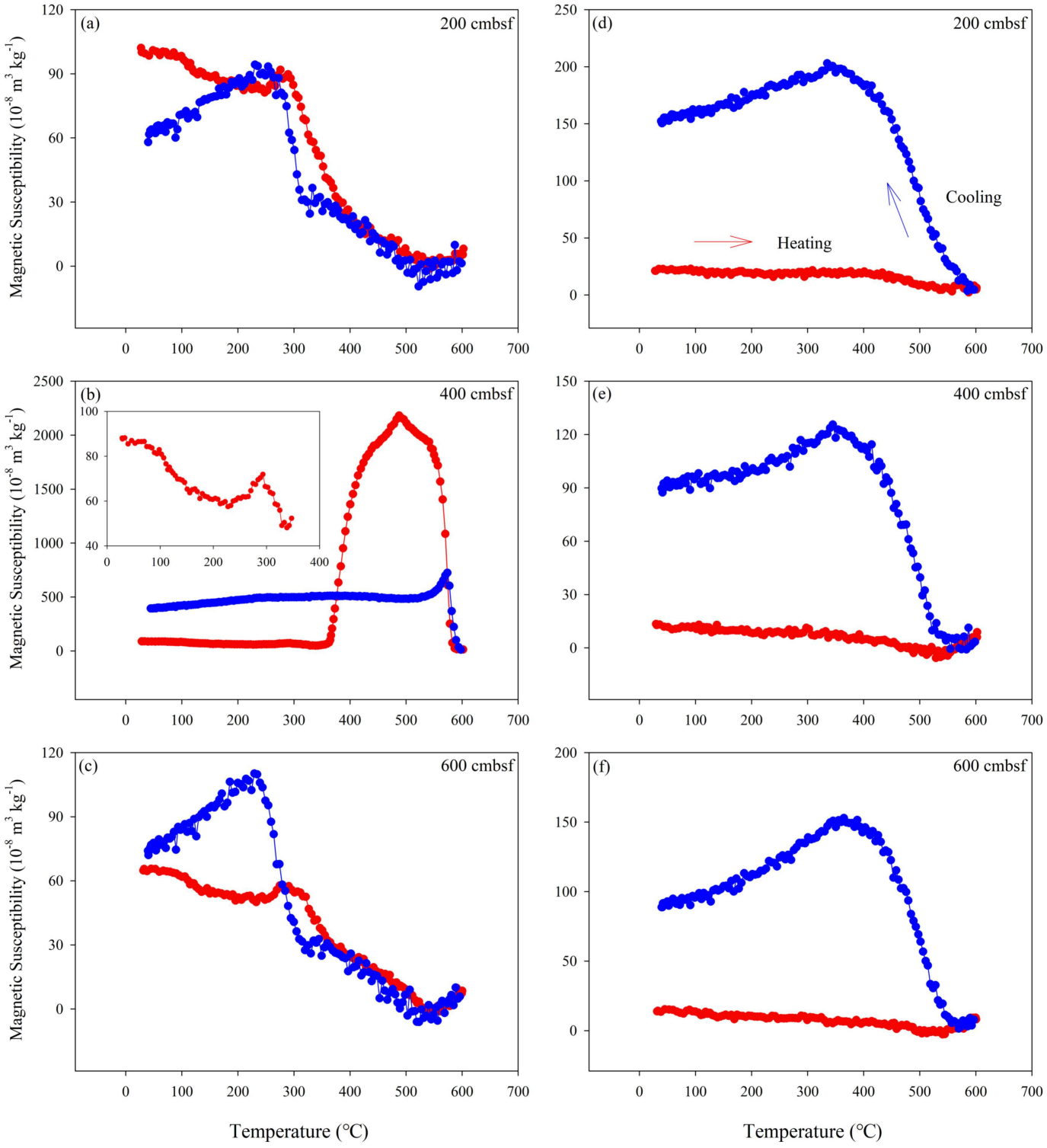
MRS-CS-05
MRS-CS-16
(a)
200 cmbsf
(b)
400 cmbsf
(c)
600 cmbsf
(d)
200 cmbsf
Cooling
Heating
(e)
400 cmbsf
(f)
600 cmbsf
Magnetic Susceptibility (10^{-8} m^3 kg^{-1})
Temperature (°C)

Figure 3

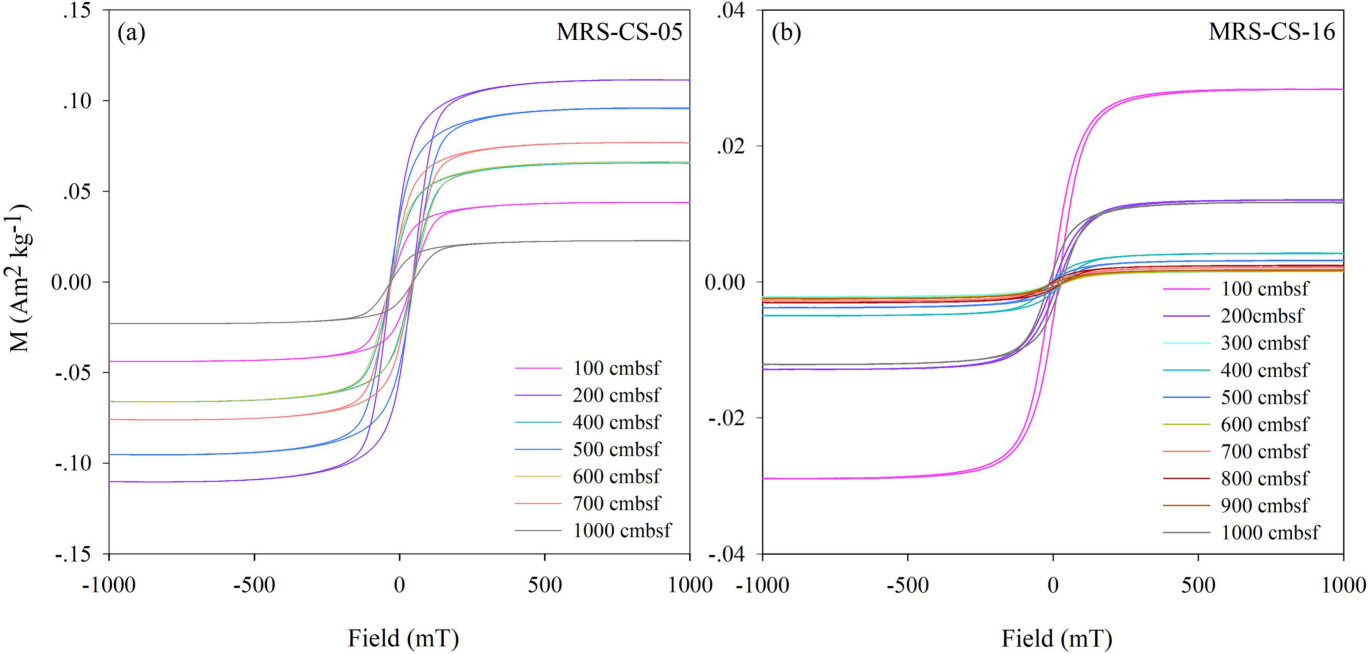
(a)
MRS-CS-05
(b)
MRS-CS-16
M (Am2 kg-1)
Field (mT)
Field (mT)
100 cmbsf
200 cmbsf
400 cmbsf
500 cmbsf
600 cmbsf
700 cmbsf
1000 cmbsf
100 cmbsf
200cmbsf
300 cmbsf
400 cmbsf
500 cmbsf
600 cmbsf
700 cmbsf
800 cmbsf
900 cmbsf
1000 cmbsf

Figure 4

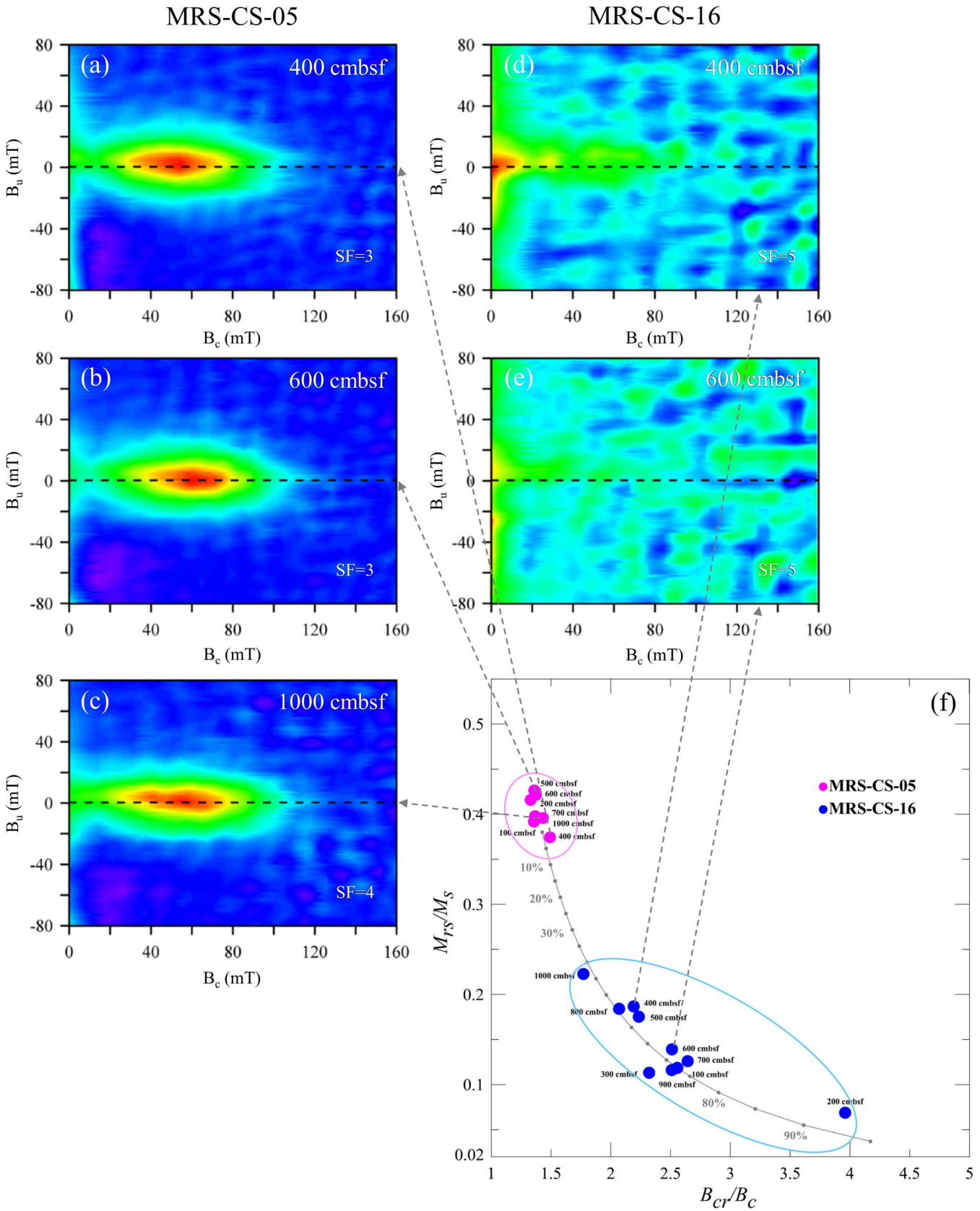
MRS-CS-05
MRS-CS-16
(a)
400 cmbsf
SF=3
(b)
600 cmbsf
SF=3
(c)
1000 cmbsf
SF=4
(d)
400 cmbsf
SF=5
(e)
600 cmbsf
SF=5
(f)
MRS-CS-05
MRS-CS-16
1500 cmbsf
600 cmbsf
200 cmbsf
700 cmbsf
1000 cmbsf
100 cmbsf
400 cmbsf
10%
20%
30%
1000 cmbsf
800 cmbsf
400 cmbsf
500 cmbsf
600 cmbsf
700 cmbsf
300 cmbsf
100 cmbsf
900 cmbsf
80%
200 cmbsf
90%
B_u (mT)
B_c (mT)
M_rs/M_s
B_cr/B_c

Figure 5

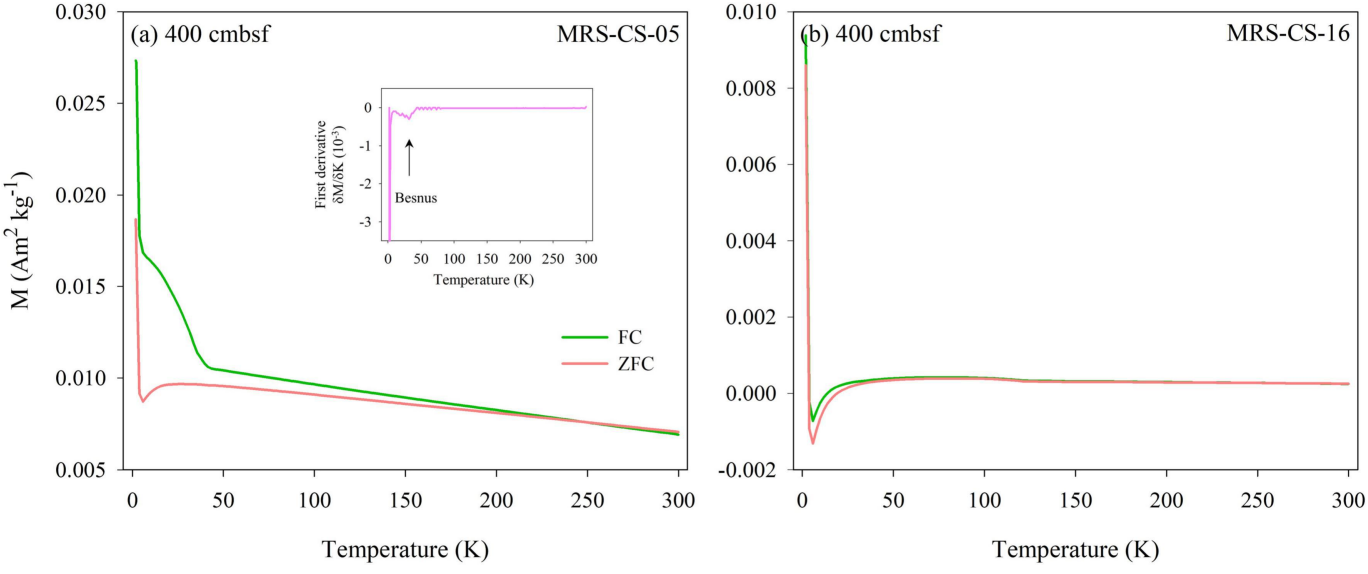
(a) 400 cmbsf
MRS-CS-05
M (Am^2 kg^{-1})
0.030
0.025
0.020
0.015
0.010
0.005
0
50
100
150
200
250
300
Temperature (K)
FC
ZFC
First derivative
δM/δK (10^{-3})
0
-1
-2
-3
Besnus
0
50
100
150
200
250
300
Temperature (K)
(b) 400 cmbsf
MRS-CS-16
0.010
0.008
0.006
0.004
0.002
0.000
-0.002
0
50
100
150
200
250
300
Temperature (K)

Figure 6

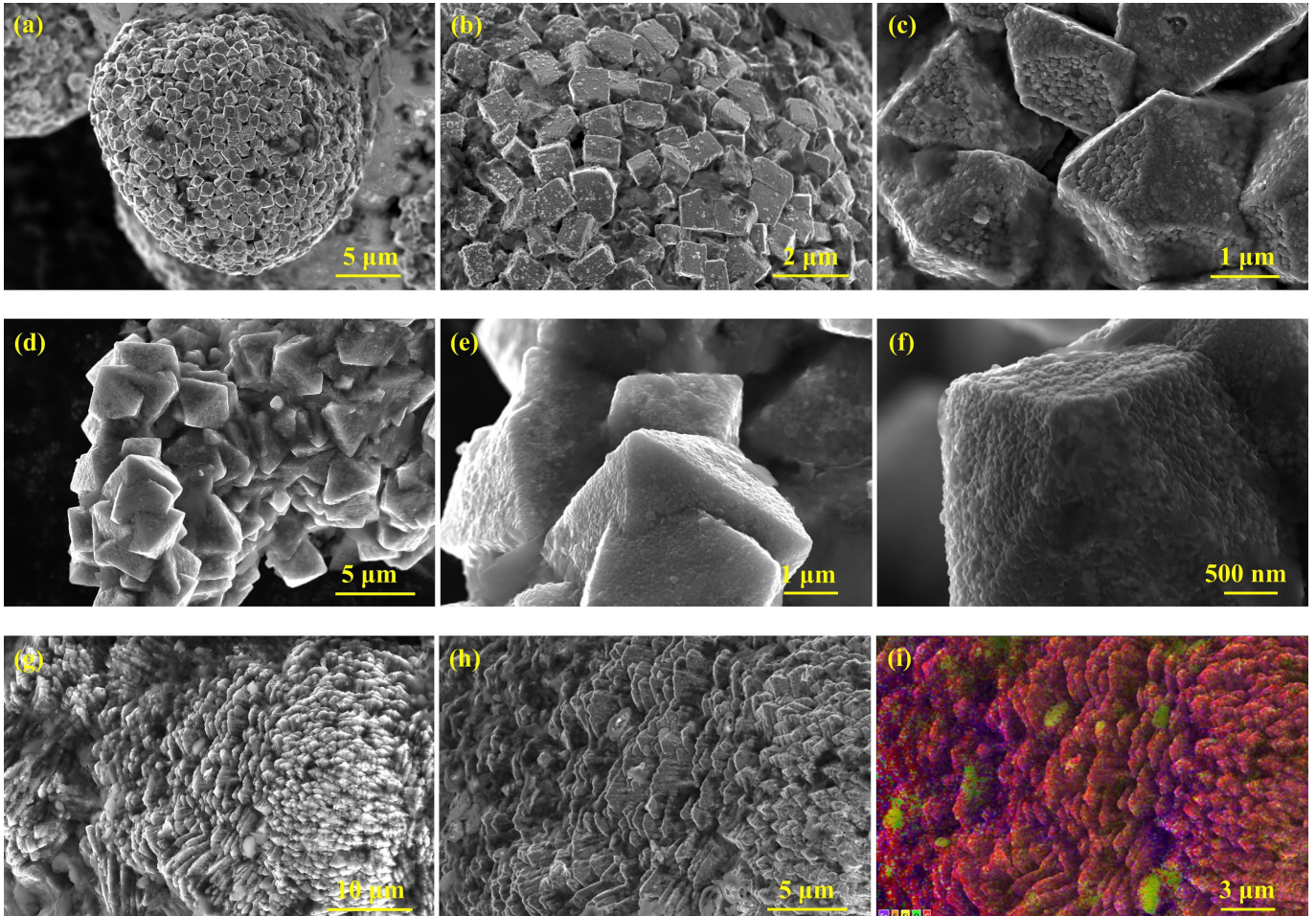

Figure 7

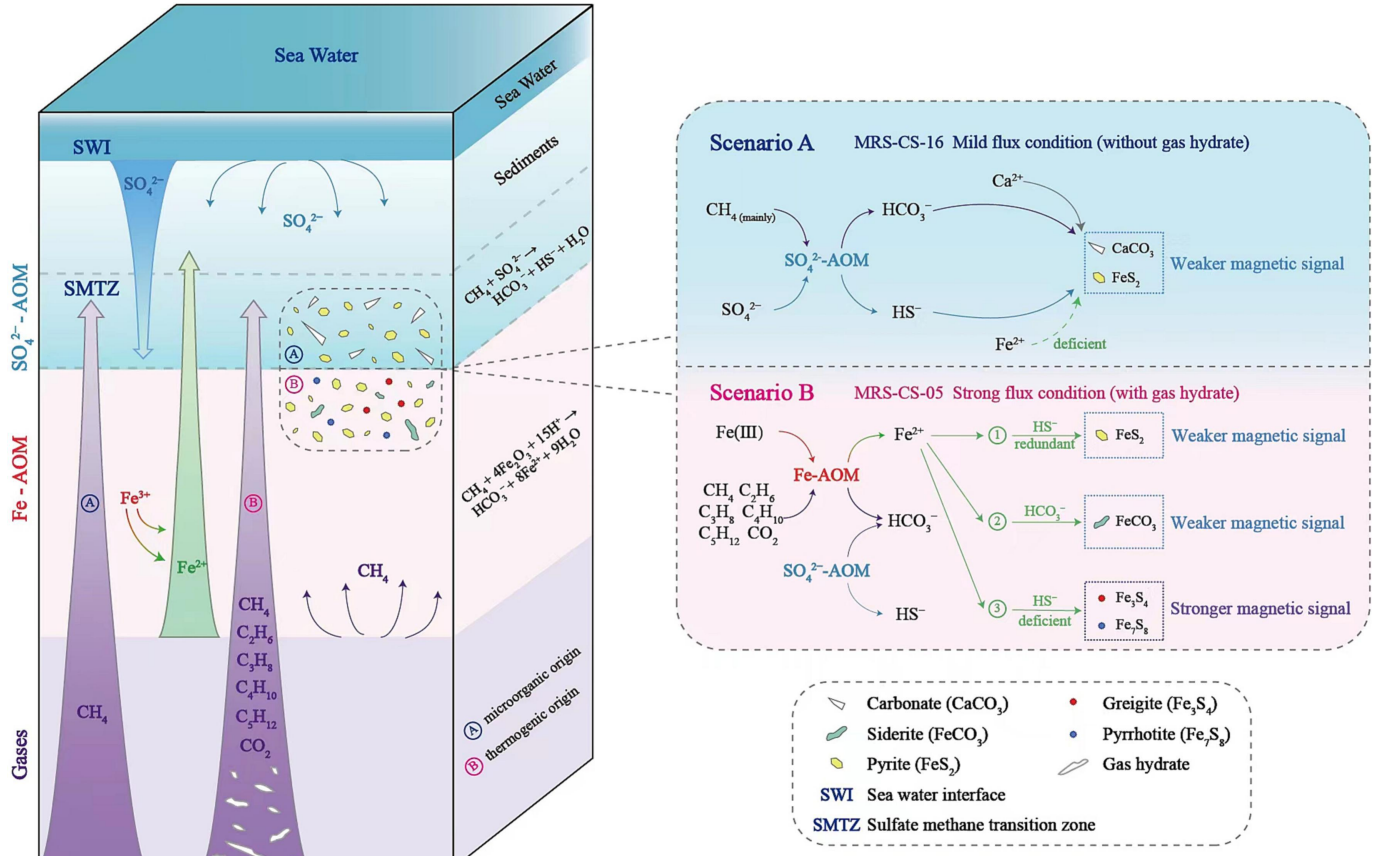
Sea Water
Sea Water
SWI
Sediments
SMTZ
SO_4^{2-} - AOM
Fe - AOM
Gases
SO_4^{2-}
SO_4^{2-}
$CH_4 + SO_4^{2-} \rightarrow HCO_3^- + HS^- + H_2O$
A
B
Fe^{3+}
Fe^{2+}
CH_4
$CH_4 + 4Fe_2O_3 + 15H^+ \rightarrow HCO_3^- + 8Fe^{2+} + 9H_2O$
CH_4
C_2H_6
C_3H_8
C_4H_{10}
C_5H_{12}
CO_2
A microorganic origin
B thermogenic origin
Scenario A
MRS-CS-16 Mild flux condition (without gas hydrate)
CH_4 (mainly)
SO_4^{2-}
SO_4^{2-}-AOM
HCO_3^-
Ca^{2+}
HS^-
Fe^{2+}
deficient
$CaCO_3$
FeS_2
Weaker magnetic signal
Scenario B
MRS-CS-05 Strong flux condition (with gas hydrate)
Fe(III)
Fe-AOM
CH_4 C_2H_6
C_3H_8 C_4H_{10}
C_5H_{12} CO_2
SO_4^{2-}-AOM
Fe^{2+}
HCO_3^-
HS^-
① HS^- redundant
② HCO_3^-
③ HS^- deficient
FeS_2
Weaker magnetic signal
$FeCO_3$
Weaker magnetic signal
Fe_3S_4
Fe_7S_8
Stronger magnetic signal
Carbonate ($CaCO_3$)
Siderite ($FeCO_3$)
Pyrite (FeS_2)
Greigite (Fe_3S_4)
Pyrrhotite (Fe_7S_8)
Gas hydrate
SWI Sea water interface
SMTZ Sulfate methane transition zone

Figure 8